



# MIT Open Access Articles

*New insight into the material parameter B to understand the enhanced thermoelectric performance of  $Mg_{2}S_{n-1-x-y}Ge_{x}Sb_{y}$*

The MIT Faculty has made this article openly available. **Please share** how this access benefits you. Your story matters.

<b>Citation</b>	Liu, Weishu et al. "New Insight into the Material Parameter B to Understand the Enhanced Thermoelectric Performance of $Mg_{2}S_{n-1-x-y}Ge_{x}Sb_{y}$ ." Energy Environ. Sci. 9.2 (2016): 530–539.
<b>As Published</b>	<a href="http://dx.doi.org/10.1039/C5EE02600H">http://dx.doi.org/10.1039/C5EE02600H</a>
<b>Publisher</b>	Royal Society of Chemistry
<b>Version</b>	Author's final manuscript
<b>Citable link</b>	<a href="http://hdl.handle.net/1721.1/108547">http://hdl.handle.net/1721.1/108547</a>
<b>Terms of Use</b>	Creative Commons Attribution-Noncommercial-Share Alike
<b>Detailed Terms</b>	<a href="http://creativecommons.org/licenses/by-nc-sa/4.0/">http://creativecommons.org/licenses/by-nc-sa/4.0/</a>

# New insight into the material parameter $B$ to understand the enhanced thermoelectric performance of $\text{Mg}_2\text{Sn}_{1-x-y}\text{Ge}_x\text{Sb}_y$

Weishu liu,<sup>a</sup> Jiawei Zhou,<sup>b</sup> Qing Jie,<sup>a</sup> Yang Li,<sup>c</sup> Hee Seok Kim,<sup>a</sup> Jiming Bao,<sup>c</sup> Gang Chen<sup>b\*</sup> and Zhifeng Ren<sup>a\*</sup>

Historically, material parameter  $B$  incorporating weighted mobility and lattice thermal conductivity has guided the exploration of novel thermoelectric materials. However, the conventional definition of  $B$  neglects the bipolar effect which can dramatically change the thermoelectric energy conversion efficiency at high temperatures. In this paper, a generalized material parameter  $B^*$  is derived, which connects weighted mobility, lattice thermal conductivity, and band gap. Based on the new parameter  $B^*$ , we explain the successful tuning of the electron and phonon transport in  $\text{Mg}_2\text{Sn}_{1-x-y}\text{Ge}_x\text{Sb}_y$ , with an improved  $ZT$  value from 0.6 in  $\text{Mg}_2\text{Sn}_{0.99}\text{Sb}_{0.01}$  to 1.4 in  $\text{Mg}_2\text{Sn}_{0.73}\text{Ge}_{0.25}\text{Sb}_{0.02}$ . We uncover that the Ge alloying approach simultaneously improves all the key variables in the material parameter  $B^*$ , with a  $\sim 25\%$  enhancement in the weighted mobility,  $\sim 27\%$  band gap widening, and  $\sim 50\%$  reduction in the lattice thermal conductivity. We show that higher generalized parameter  $B^*$  leads to a higher optimized  $ZT$  in  $\text{Mg}_2\text{Sn}_{0.73}\text{Ge}_{0.25}\text{Sb}_{0.02}$ , and some common thermoelectric materials. The new parameter  $B^*$  provides a better characterization of material's thermoelectric transport, particularly at high temperatures, and therefore can facilitate the search of good thermoelectric materials.

## Broader Context

Thermoelectric conversion involves the transport of electrons and phonons. It has been very challenging to synergistically tune the macro thermoelectric transport parameters: electrical conductivity, thermal conductivity, and Seebeck coefficient as these properties are coupled to each other. Recently, we have achieved a significant enhancement in the thermoelectric performance of  $\text{Mg}_2\text{Sn}$  by partially substituting Sn with Ge and doping Sb. The new material  $\text{Mg}_2\text{Sn}_{0.728}\text{Ge}_{0.25}\text{Sb}_{0.022}$  has a high average  $ZT$  (0.9) and power factor ( $52 \mu\text{W cm}^{-1} \text{K}^{-2}$ ) in the temperature range of 25–450 °C, with favourably high efficiency and large output power density. The  $ZT$  improvement is understood through a generalized material parameter  $B^*$ , which connects weighted mobility, lattice thermal conductivity, and band gap. A higher  $B^*$  is desired for higher  $ZT$ . The new parameter will help guide the optimizations of known materials by synergistically tailoring these fundamental parameters to enhance their thermoelectric performance, and the search of new materials by using it as new scale.

## 1. Introduction

The efficiency of thermoelectric power generation is governed by the Carnot efficiency and dimensionless figure of merit ( $ZT$ ) of the material.  $ZT$  is defined as  $ZT = (S^2\sigma/\kappa)T$ , where  $S$ ,  $\sigma$ ,  $\kappa$ , and  $T$  are the Seebeck coefficient, electrical conductivity, thermal conductivity, and absolute temperature, respectively.<sup>1</sup>  $ZT$  value strongly depends on the carrier concentration. Optimization of the carrier concentration leads to optimized reduced Fermi energy ( $\zeta_f = E_f/k_B T$ ) close to the band edge  $E_c$  for n-type and  $E_v$  for the p-type semiconductor,<sup>2</sup> where the energy is measured from  $E_c$  ( $E_v$ ) for the n-type (p-type) semiconductor. However, the maximum  $ZT$  is limited by the interdependence of  $S$ ,  $\sigma$ , and  $\kappa$ .<sup>3</sup> In evaluating material's thermoelectric performance, a dimensionless material parameter  $B$ , proposed first by Chasmar and Stratton from a single parabolic band model in the nondegenerate limit, has proven to be very useful.<sup>4-8</sup>

$$B = 5.745 \times 10^{-6} \frac{\mu (m^*/m_0)^{3/2}}{\kappa_{lat}} T^{5/2}, \quad (1)$$

where  $m^*$ ,  $m_0$ ,  $\mu$ ,  $\kappa_{lat}$ , and  $T$  are the carrier effective mass, free electron mass, carrier mobility, lattice thermal conductivity, and absolute temperature, respectively. All the parameters defined in Eq. (1) are expressed in SI units, i.e.,  $\mu$  in  $\text{m}^2 \text{V}^{-1} \text{s}^{-1}$  and  $\kappa_{lat}$  in  $\text{W m}^{-1} \text{K}^{-1}$ . The product of  $\mu$  and  $(m^*/m_0)^{3/2}$  was commonly called

weighted mobility and will be denoted as  $U$ . A large material parameter  $B$  usually corresponds to a high  $ZT$  value at the optimized  $\zeta_f$ . The power of this parameter lies in that it provides a clear guidance to identify better thermoelectric materials instead of checking all the transport properties ( $S$ ,  $\sigma$  and  $\kappa$ ), one should look for materials with a high weighted mobility  $U$  and low lattice thermal conductivity  $\kappa_{lat}$ , which are less dependent on each other. Furthermore, the material parameter  $B$  was generalized to take into account the effect of alloying scattering,<sup>9</sup> as well as additional electron (hole) bands.<sup>10</sup> Despite the insightful understandings gained from the parameter  $B$ , Eq. (1) implies that this parameter increases with the temperature continuously, while  $ZT$  of most real materials drops at high temperatures due to the bipolar effect. It has been known that materials with small energy band gap ( $E_g$ ) suffer more from the bipolar effect due to the decreased Seebeck coefficient and increased thermal conductivity.<sup>11</sup> Previous work has shown that the optimized band gap is related to the temperature, i.e.,  $E_g = 4-10 k_B T$ .<sup>4, 12, 13</sup> For given material parameters  $B$  and temperature  $T$ , the optimized  $ZT$  with respect to the carrier concentration increases with the band gap and becomes saturated as  $E_g > 10 k_B T$  for both direct and indirect band gaps.<sup>13, 14</sup> However, a generalized material parameter similar to  $B$  is missing that permits the evaluation of material's thermoelectric performance by exploring the tradeoff among  $U$ ,  $\kappa_{lat}$ , and  $E_g$  in a more fundamental way rather than examining  $S$ ,  $\sigma$ , and  $\kappa$ .

Nano approach has worked for most of the thermoelectric materials because the scattering centers scatter phonons more than electrons.<sup>15, 16</sup> Recently, a first-principles-based simulations for silicon have shown that the length span of the mean free path of phonons is much longer than that of electrons, which give a good explanation for enhanced ZT from the nano approach strategy.<sup>17</sup> However, further reduction of  $\kappa_{lat}$  may lead to reduced  $U$ , when the average distance between two neighbor scattering centers becomes comparable to the electron mean free path. Different strategies have been developed to reduce the decrease of the carrier mobility when applying the nanostructuring approach to reduce  $\kappa_{lat}$ , such as modulation doping,<sup>18</sup> ordered nano inclusion,<sup>3</sup> re-oriented grains,<sup>19</sup> and better alignment of band edge offsets between the inclusions and matrix.<sup>20</sup> In another direction different from the phonon engineering, increased electronic density-of-states due to resonant dopants,<sup>21-23</sup> and the band convergence effect<sup>24, 25</sup> has been used to improve the power factor by increasing the effective mass. Furthermore, there is one constraint between  $E_g$  and  $\kappa_{lat}$ . For two compounds with similar crystalline structures, the one composed of lighter elements usually has larger  $E_g$  and higher  $\kappa_{lat}$  due to stronger chemical bonding.<sup>26</sup> One way to go beyond this limit is to have complex crystalline structure as complex crystal structures have more optical phonons that do not contribute much to heat conduction and yet can scatter acoustic phonons, leading to a lower lattice thermal conductivity.<sup>27</sup> Despite various strategies mentioned above, there does not exist a unified parameter connecting the three fundamental parameters  $U$ ,  $\kappa_{lat}$ , and  $E_g$  to guide the improvement of ZT.

In this work, we derive a generalized material parameter  $B^*$ , which is proportional to  $U$  and  $E_g$  while inversely proportional to  $\kappa_{lat}$ , and apply it to study the enhanced thermoelectric performance of alloyed Mg<sub>2</sub>Sn. Mg<sub>2</sub>Sn is a semiconductor with a narrow band gap of 0.26 eV,<sup>28</sup> which has recently been investigated in the composition of Mg<sub>2</sub>Sn<sub>0.6</sub>Si<sub>0.4</sub>, showing a ZT of 1.1-1.3.<sup>29-34</sup> In our previous work,<sup>35</sup> we successfully synthesized Mg<sub>2</sub>Sn using mechanical ball milling technique followed by hot pressing, which showed a high carrier mobility of  $\sim 90 \text{ cm}^2 \text{ V}^{-1} \text{ s}^{-1}$  at a high doping concentration ( $n \sim 1.8 \times 10^{20} \text{ cm}^{-3}$ ). A record ZT of 1.4 at 450 °C and a peak power factor (PF) of  $55 \mu\text{W cm}^{-1} \text{ K}^{-2}$  at 350 °C were obtained in Mg<sub>2</sub>Sn<sub>0.728</sub>Sb<sub>0.022</sub>Ge<sub>0.25</sub> with a small amount of extra Mg. The thermoelectric performance of this material surpassed other materials' operating in the temperature range of 50-450 °C in terms of both the efficiency and output power. In this paper, we systematically investigated the alloying effect of Ge in Mg<sub>2</sub>Sn<sub>1-x-y</sub>Ge<sub>x</sub>Sb<sub>y</sub> in terms of the generalized material parameter  $B^*$ . It is found that the ZT enhancement due to Ge alloying can be understood as a synergetic effect of a  $\sim 25\%$  enhancement in  $U$ ,  $\sim 27\%$  widening in  $E_g$  and  $\sim 50\%$  reduction in  $\kappa_{lat}$ . Furthermore, the connection between the material parameter  $B^*$  and peak ZT for some classic materials, including CoSb<sub>3</sub>, Bi<sub>2</sub>Te<sub>3</sub> and PbTe, were also discussed.

## 2. Experimental details

**Synthesis.** The synthesis process of Mg<sub>2</sub>Sn<sub>1-x-y</sub>Ge<sub>x</sub>Sb<sub>y</sub> ( $x = 0-0.3$ ,  $y = 0-0.025$ ) was similar to our previous work. Elemental powders of Mg, Sn, Ge, and Sb were used for ball milling and then hot pressing at 600-750 °C for 2 minutes.

**Thermoelectric transport properties.** The electrical resistivity was measured by a DC-current four-point method, while the

Seebeck coefficient was determined by the slope of the voltage difference versus temperature difference curve based on a static temperature difference method. The simultaneous measurement of electrical resistivity and Seebeck coefficient was conducted on a commercial system (ZEM-3, ULVAC). The thermal conductivity was calculated from the relationship  $\kappa = DC_p d$ , where  $D$ ,  $C_p$ , and  $d$  are the thermal diffusivity, specific heat, and volumetric density, respectively. The thermal diffusivity was measured by the laser flash method with a commercial system (LFA457, Netzsch). The specific heat capacity was determined by a differential scanning calorimeter (DSC 404 C, Netzsch). The volumetric density was measured by the Archimedes method. The measurement of Hall coefficient,  $R_H$ , was carried out on a commercial system (PPMS, Quantum Design), with a magnetic field up to 6 T and an electrical current of 10-20 mA.

**Band gap measurement.** Fourier transform infrared spectroscopy (FTIR) is performed to derive the optical band gap based on the Kramers-Kronig analysis of the reflectance. The FTIR is conducted on an infrared spectroscopy (iS50, Thermo Nicolet) with DTGS detector at room temperature in the range of 4000 to 400  $\text{cm}^{-1}$  with a resolution of 4  $\text{cm}^{-1}$ . The reflectance spectra  $R(\omega)$  was taken with an angle of  $10^\circ$  near normal incident direction.

**Theoretical calculation.** First principles calculations are performed for the band structures of Mg<sub>2</sub>Sn and Mg<sub>2</sub>Ge using the linearized augmented plane-wave (LAPW) method<sup>36</sup> as implemented in the WIEN2K simulation package.<sup>37</sup> The generalized gradient approximation (GGA) of Perdew, Burke, and Ernzerhof<sup>38</sup> is used with a Brillouin zone sampling including more than 200 **k**-points in the irreducible wedge of the Brillouin zone. The newly-developed TB-mBJ function<sup>39</sup> is also applied for improving the calculation of the band structure and especially the band gap. Basis sets are determined by  $R_{MT}K_{max} = 8$ , where  $R_{MT}$  is the smallest muffin-tin radius, and  $K_{max}$  is the maximum value of reciprocal-lattice vectors. The LAPW sphere radii for Mg, Sn, and Ge are chosen to be  $2.2a_0$ , where  $a_0$  is the lattice constant determined from the experiment. Besides, the relativistic effects for the valence electrons are included at the scalar relativistic level.

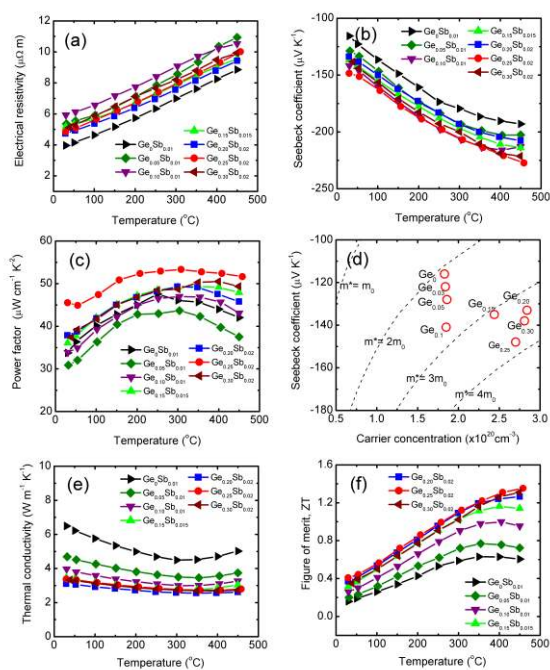


**Fig. 1.** Thermoelectric properties of  $\text{Mg}_2\text{Sn}_{1-x-y}\text{Ge}_x\text{Sb}_y$ . (a) Electrical resistivity, (b) Seebeck coefficient, (c) power factor, (d) Seebeck coefficient versus carrier concentration, (e) thermal conductivity, and (f)  $ZT$ .

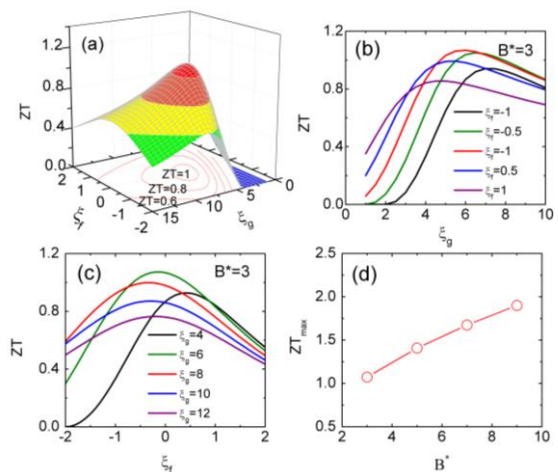
### 3. Results

Fig. 1 shows the temperature dependent thermoelectric properties of  $\text{Mg}_2\text{Sn}_{1-x-y}\text{Ge}_x\text{Sb}_y$  ( $x = 0, 0.05, 0.1, 0.15, 0.2, 0.25$ , and  $0.3$ ,  $y = 0.01, 0.015$ , and  $0.02$ ). All the samples show almost linearly increased electrical resistivity and Seebeck coefficient below  $300\text{ }^\circ\text{C}$ , demonstrating a behavior of degenerate semiconductor, as shown in Fig. 1(a-b). The Fermi energy ( $E_f$ ) calculated from the Seebeck coefficient is  $0.031\text{--}0.049\text{ eV}$ , equal to  $1.2\text{--}1.9 k_B T$  at room temperature, above the bottom of the conduction band,  $E_c$ . Above  $300\text{ }^\circ\text{C}$ , the Seebeck coefficient of  $\text{Mg}_2\text{Sn}_{1-x-y}\text{Ge}_x\text{Sb}_y$  with  $x = 0$  and  $0.05$  shows saturated characteristics while that with  $x = 0.25$  and  $0.30$  continues to be linearly temperature dependent. Among the samples,  $\text{Mg}_2\text{Sn}_{0.73}\text{Ge}_{0.25}\text{Sb}_{0.02}$  shows the highest  $PF$ ,  $43\text{ }\mu\text{W cm}^{-1}\text{ K}^{-2}$  near room temperature and over  $50\text{ }\mu\text{W cm}^{-1}\text{ K}^{-2}$  in a wide temperature range, as shown in Fig. 1 (c). Here, Sb was the electron donor. An approximate linear relationship between the carrier concentration and Sb content was observed in  $\text{Mg}_2\text{Sn}_{1-x-y}\text{Ge}_x\text{Sb}_y$ , which indicates  $\sim 1\text{ carr./Sb}$ , as shown in Fig. S1 (a-b) (ESI<sup>†</sup>). It is noted that the free charge transferring from Sb atom is independent of the Ge content (Fig. S1 (c), ESI<sup>†</sup>). Fig. 1(d) plots the Seebeck coefficient versus carrier concentration near room temperature for  $\text{Mg}_2\text{Sn}_{1-x-y}\text{Ge}_x\text{Sb}_y$ . For samples with  $y = 0.01$ , Seebeck coefficient increases from  $-116\text{ }\mu\text{V K}^{-1}$  for  $x = 0$  to  $-141\text{ }\mu\text{V K}^{-1}$  for  $x = 0.1$ . Furthermore, for samples with  $x = 0.1$  and  $y = 0.01$ ,  $x = 0.15$  and  $y = 0.015$ ,  $x = 0.2$  and  $y = 0.02$ , there is only a small change in the Seebeck coefficient while a significant increase in carrier concentration from  $1.68 \times 10^{20}\text{ cm}^{-3}$  ( $x = 0.1, y = 0.01$ ) to  $2.70 \times 10^{20}\text{ cm}^{-3}$  ( $x = 0.25, y = 0.02$ ). As Ge content increases beyond  $0.2$ , a maximum Seebeck and the highest  $PF$  were achieved in sample  $\text{Mg}_2\text{Sn}_{1-x-y}\text{Ge}_x\text{Sb}_y$  with  $x = 0.25$  and  $y = 0.02$ . The Ge

content variation in the carrier effective mass of  $\text{Mg}_2\text{Sn}_{1-x-y}\text{Ge}_x\text{Sb}_y$  implies that the band structure significantly changes with Ge, which will be discussed in the next section. Fig. 1 (e) shows a significant decrease in thermal conductivity with increased Ge content in  $\text{Mg}_2\text{Sn}_{1-x-y}\text{Ge}_x\text{Sb}_y$ . The corresponding thermal diffusivity and specific heat of  $\text{Mg}_2\text{Sn}_{1-x-y}\text{Ge}_x\text{Sb}_y$  are shown in Fig. S2 (a-b) (ESI<sup>†</sup>). Due to the increased  $PF$  and the decreased thermal conductivity, the  $ZT$  value is significantly enhanced from  $0.6$  for  $x = 0$  to around  $1.4$  for  $x = 0.25$ , as shown in Fig. 1 (f). The sample with higher Ge content ( $x = 0.3$ ) shows slightly lower  $ZT$  value due to a lower  $PF$ . The reproducibility of samples  $\text{Mg}_2\text{Sn}_{0.75-y}\text{Ge}_{0.25}\text{Sb}_y$  with two different carrier concentrations of  $2.7 \times 10^{20}$  ( $y = 0.02$ ) and  $3.0 \times 10^{20}\text{ cm}^{-3}$  ( $y = 0.022$ ) is confirmed by three batches for each composition, as shown in Fig. S3 (ESI<sup>†</sup>). The room temperature Seebeck coefficient is around  $-147\text{ }\mu\text{V K}^{-1}$  for the samples with carrier concentration of  $2.7 \times 10^{20}\text{ cm}^{-3}$ , while  $-137\text{ }\mu\text{V K}^{-1}$  for the samples with carrier concentration of  $3.0 \times 10^{20}\text{ cm}^{-3}$ . A good reproducibility was achieved for both compositions. The coefficient of variation of thermoelectric transport properties from batch to batch is less than  $5\%$ . The average  $ZT$ s for both compositions are close to  $1.4$  at  $450\text{ }^\circ\text{C}$ .

### 4. Discussion

In the previous section, it is shown how to chemically tune the composition of  $\text{Mg}_2\text{Sn}_{1-x-y}\text{Ge}_x\text{Sb}_y$  to achieve high  $ZT$  and  $PF$ . In this section, we will discuss the physical mechanism of the enhanced  $ZT$  due to the alloying of Ge in  $\text{Mg}_2\text{Sn}$ . The generalized material parameter  $B^*$  will be derived, and the  $ZT$  enhancement is then understood in terms of the fundamental parameters  $U$ ,  $\kappa_{lat}$ , and  $E_g$ .



**Fig. 2.** Theoretical  $ZT$  as a function of  $\xi_f$ ,  $\xi_g$ , and  $B^*$ . (a) A 3D plot of  $ZT$  versus  $\xi_f$  and  $\xi_g$  with a fixed  $B^* = 3$ , (b)  $ZT$  versus  $\xi_g$  with fixed  $B^* = 3$  and  $\xi_f = -1, -0.5, 0, 0.5, 1$ ; (c)  $ZT$  versus  $\xi_f$  with fixed  $B^* = 3$  and  $\xi_g = 4, 6, 8, 10, 12$ ; (d) maximum  $ZT$  as a function of  $B^*$ .

#### 4.1 Generalized Material parameter $B^*$

The original definition of material parameter  $B$  was firstly introduced by Chasmar and Stratton through expressing the figure

of merit using Fermi–Dirac statistics with non-degenerate approximation as follows,<sup>4,5</sup>

$$ZT = \frac{S^2 \sigma T}{\kappa_{lat} + \kappa_{carr}} = \frac{S^2}{\kappa_{lat} / \sigma T + L} = \frac{\left[ (s+5/2) - \xi_f \right]^2}{\left[ B \exp(\xi_f) \right]^{-1} + L} \quad (2)$$

$$B = \left( \frac{k_B}{e} \right)^2 \frac{\sigma_0}{\kappa_{lat}} T \quad (3)$$

$$\sigma_0 = 2e\mu \left( \frac{2\pi m^* k_B T}{h^2} \right)^{3/2} \quad (4)$$

where  $s$ ,  $L$ ,  $\kappa_{lat}$ ,  $\kappa_{carr}$  are the scattering factor, Lorenz number, lattice thermal conductivity and carrier thermal conductivity. The definition of  $s$  is based on the relaxation time approximation for the electronic transport. For example,  $s = -1/2$  for the acoustic phonon dominant scattering case. By using the SI units for the free electron charge ( $e$ ), free electron mass ( $m_0$ ), Boltzmann constant ( $k_B$ ), Plank constant ( $h$ ), Eq. (3) turns into Eq. (1). In Eq. (2),  $ZT$  is only considered as a function of the reduced Fermi level  $\xi_f$ , while material parameter  $B$  was considered as an independent parameter of  $\xi_f$ . A higher  $B$  usually corresponds to a higher  $(ZT)_{max}$  at optimized  $\xi_f^*$ . It is noted that the original definition of  $B$  includes variable  $T$ , which incorrectly indicates that  $B$  increases with temperature  $T$  continuously. However, the  $ZT$  of a real material drops at high temperatures due to the bipolar effect. To take into account the bipolar effect, it is necessary to use a two band model.<sup>11</sup> For an artificial material with electrons as the major carrier while holes as the minor carrier, Eq. (2) can be generalized into the following form (see details in ESI†),

$$ZT = \frac{\left( \delta_e - \xi_{f,e} - \frac{\delta_e + \delta_h + \xi_g}{1+1/\gamma} \right)^2 (1+\gamma)}{\left( \frac{B}{B^*} \frac{F_{1/2}(\xi_{f,e})}{\Gamma(3/2)} \right)^{-1} + \frac{(\delta_e + \delta_h + \xi_g)^2}{1+1/\gamma} + L_e + \gamma L_h} \quad (5)$$

for which we have defined

$$\delta_i = \frac{(s+5/2) F_{s+3/2}(\xi_{f,i})}{(s+3/2) F_{s+1/2}(\xi_{f,i})}, i = e, h \quad (6)$$

$$L_i = \left( \frac{k_B}{e} \right)^2 \left( \frac{(s+7/2) F_{s+3/2}(\xi_{f,i})}{(s+3/2) F_{s+1/2}(\xi_{f,i})} - \left( \frac{(s+5/2) F_{s+3/2}(\xi_{f,i})}{(s+3/2) F_{s+1/2}(\xi_{f,i})} \right)^2 \right) \quad (7)$$

$$\gamma = \frac{\mu_h (m_h^*)^{3/2} F_{1/2}(\xi_{f,e})}{\mu_e (m_e^*)^{3/2} F_{1/2}(\xi_{f,h})} = \frac{U_h}{U_e} \frac{F_{1/2}(\xi_{f,e})}{F_{1/2}(\xi_{f,h})} \quad (8)$$

where  $F_n(\xi_f)$  is the  $n^{\text{th}}$ -order Fermi integral defined as

$$F_n(\xi_f) = \int_0^\infty \frac{\chi^n}{1 + e^{\chi - \xi_f}} d\chi \quad (9)$$

and  $\xi_g = E_g/k_B T$  is the reduced band gap. The subscript  $i = e$  or  $h$  represents the electrons and holes respectively, with the reduced Fermi level  $\xi_{f,e}$  ( $\xi_{f,h}$ ) measured from conduction band edge  $E_c$  (valence band edge  $E_v$ ). According to Simon's early work,<sup>11</sup>  $\xi_{f,e}$  and  $\xi_{f,h}$  can be described by the reduced Fermi level ( $\xi_f$ ) of the major carrier band and the reduced band gap  $\xi_g$ . For an artificial n-type semiconductor, we have  $\xi_{f,e} = \xi_f$  and  $\xi_{f,h} = -\xi_f - \xi_g$ . This relation will be used to replace  $\xi_{f,e}$  and  $\xi_{f,h}$  hereafter. Furthermore, the ratio  $U_h/U_e$  and scattering factor  $s$  are considered as constants for convenience in this paper. It is noted that the form of Eq. (5)

is different from the one Mahan derived, in which a concept of minimum electrical conductivity was adopted.<sup>13</sup> Eq. (5) suggests that the negative impact of the bipolar effect comes from the terms containing  $\xi_g$ . If we fix the parameters of  $B$ ,  $T$ , and  $s$ , and consider  $E_g$  and  $\xi_f$  as the tuning variables for  $ZT$ , we reproduced Mahan's results: the optimized  $ZT$  with respect to  $\xi_f$  increases with the band gap and saturates around  $E_g \sim 10 k_B T$  as shown in Fig. S4 (ESI†). It is noted that the saturated  $ZT$  depends not only on material parameter  $B$ , but also on  $U_h/U_e$  and  $s$ .

However, the above analysis has to treat  $E_g$  separately from the material parameter  $B$ . Here we would like to explore whether we can define a parameter similar to  $B$  but including  $U$ ,  $\kappa_{lat}$ , and  $E_g$  altogether, thereby simplifying the evaluation of material's thermoelectric performance. From experimental results,  $ZT$  is usually considered as a function of the doping concentration and temperature, *i.e.*,  $ZT = f_1(N_D, T)$  for a given set of ( $U$ ,  $\kappa_{lat}$ , and  $E_g$ ). In our theoretical formalism,  $N_D$  can be described by  $\xi_f$ , and hence  $ZT$  as function of  $\xi_f$  and  $T$  is expressed by Eq. (2-4) for a single band model with a non-degenerate approximation, and by Eq. (5-8) for a two band model. Furthermore, we use the reduced band gap  $\xi_g = E_g/k_B T$  to non-dimensionalize the temperature, which changes the independent variables of  $ZT$  from ( $\xi_f$ ,  $T$ ) to ( $\xi_f$ ,  $\xi_g$ ), and therefore Eq. (5) turns into,

$$ZT = \frac{\left( \delta_e - \xi_f - \frac{\delta_e + \delta_h + \xi_g}{1+1/\gamma} \right)^2 (1+\gamma)}{\left( (B^*) \frac{F_{1/2}(\xi_f)/\Gamma(3/2)}{\xi_g} \right)^{-1} + \frac{(\delta_e + \delta_h + \xi_g)^2}{1+1/\gamma} + \left( \frac{e}{k_B} \right)^2 (L_e + \gamma L_h)} \quad (10)$$

with

$$B^* = \frac{1}{k_B} \left( \frac{e}{k_B} \right)^2 \frac{\sigma_{0,e}}{\kappa_{lat}} E_{g\_joule} \quad (11)$$

where  $B^*$  is defined as the generalized material parameter, and  $E_{g\_joule}$  is the band energy gap in J as SI unit. The new definition of the material parameter  $B^*$  overcomes the drawback of the conventional definition (Eq. (3)) that continuously increases with increasing  $T$ . For a given generalized material parameter  $B^*$ ,  $ZT$  can be now considered as a function of the reduced Fermi level and the reduced band gap, *i.e.*,  $ZT = f_3(\xi_f, \xi_g)$ . Fig. 2 plots the theoretical  $ZT$  as a function of  $\xi_f$  and  $\xi_g$  with assumptions of  $s = -1/2$  and  $U_e = U_h$ . It is clearly shown that  $ZT$  has a maximal value with respect to  $\xi_f$  and  $\xi_g$  for a given generalized material parameter  $B^*$ . At  $B^* = 3$ , the optimized  $\xi_f$  and  $\xi_g$  for maximizing  $ZT$  are close to  $-0.1$  and  $6$ , respectively, as shown in Fig. 2(a). If only  $\xi_g$  is considered as the tuning variable, the optimized  $\xi_g$  changes from  $4$  to  $7$  with  $\xi_f$  varying from  $1$  to  $-1$  as shown in Fig. 2(b). Here, we want to discuss the origin of the qualitative difference in terms of the optimized  $ZT$  with respect to the reduced band gap  $\xi_g$  between our results (an optimal point) and Mahan's work (saturated behavior). In Mahan's work, the optimized  $\xi_g$  is derived by considering  $E_g$  as a variable while  $T$  is a constant, essentially examining material's properties at a given temperature. In contrast, we optimize  $\xi_g$  assuming  $E_g$  as a constant while  $T$  as the variable, identifying the optimal temperature for a given material. Fig. 2(c) shows  $\xi_f$ -dependent  $ZT$  for different  $\xi_g$ , which suggests that the optimized  $\xi_f$  is close to  $\xi_f = 0$  and slightly depends on the  $\xi_g$ . By maximizing  $ZT$  with respect to both  $\xi_f$  and  $\xi_g$ , the final  $(ZT)_{max}$  shows a monotonous increase with increasing generalized material parameter  $B^*$ , as shown in Fig. 2(d). Combining  $E_g$  with  $U/\kappa_{lat}$ , the new material parameter  $B^*$  therefore facilitates the search of high- $ZT$  materials over the

two-dimensional (doping level and temperature) parameter space. Next, we will consider a simplification of Eq. (11). According to the definition of  $\sigma_0$ , the main term are  $(m^*)^{3/2}$ ,  $\mu$ , and  $T^{3/2}$ . It is noted that the term of  $\mu T^{3/2}$  is a temperature independent parameter for acoustic phonon scattering dominated electron transport since  $\mu$  depends on  $T^{-3/2}$ .<sup>9</sup> Therefore, we can define a new temperature-independent parameter  $U^*$ , and rewrite the dimensionless material parameter  $B^*$  as,

$$B^* = 6.668 \times 10^{-2} \frac{U^*}{\kappa_{lat}} E_{g-eV} \quad (12)$$

$$U^* = \mu (m^* / m_0)^{3/2} T^{3/2} \quad (13)$$

where  $E_{g-eV}$  is band gap in eV as the conventional unit. Furthermore, the expression of  $B^*$  clearly suggests that good thermoelectric materials should have higher  $U^*$ , larger  $E_g$ , and smaller  $\kappa_{lat}$ , which serves as signatures to understand materials' thermoelectric performance and also indicators to rationally guide the search of better thermoelectric materials.

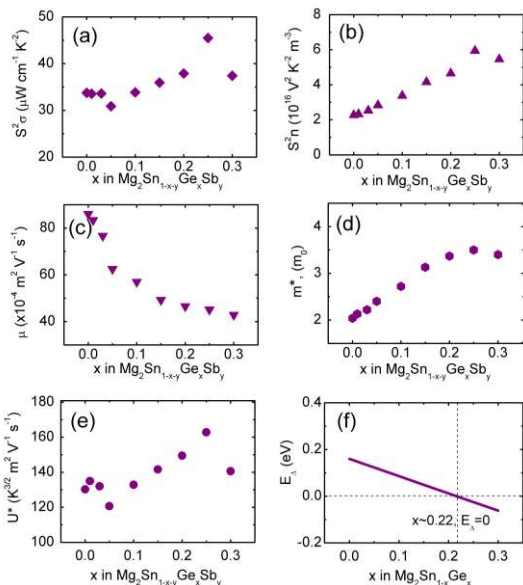


**Fig. 3.** Effect of Ge content on the thermoelectric properties of  $\text{Mg}_2\text{Sn}_{1-x}\text{Ge}_x\text{Sb}_y$ . (a) Power factor  $S^2\sigma$ , (b)  $S^2n$ , (c) carrier mobility  $\mu$ , (d) carrier effective mass  $m^*$ , (e) parameter  $U^*$ , and (f) band edge difference between two sub-conduction bands in  $\text{Mg}_2\text{Sn}_{1-x}\text{Ge}_x$ . (a-f) is the measured data in this study, while the data in (f) are from the Ref. 28 and Ref. 29.

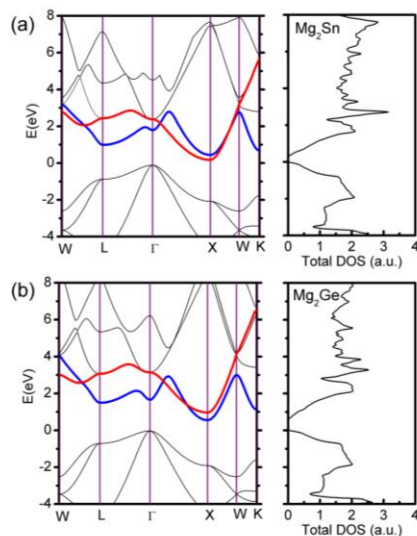


**Fig. 4.** Band structure and total density of states (DOS) of  $\text{Mg}_2\text{X}$  ( $X = \text{Sn}, \text{Ge}$ ). (a)  $\text{Mg}_2\text{Sn}$ , (b)  $\text{Mg}_2\text{Ge}$ . Two sub-conduction band edges were highlighted. The red line is denoted for  $X_H$  band, while the blue line is denoted for  $X_L$ .

#### 4.2 Enhanced power factor due to increased $U^*$

Having derived the generalized material parameter  $B^*$  in expression of  $U$ ,  $\kappa_{lab}$ , and  $E_g$  as three fundamental parameters that affect  $ZT$ , we discuss their changes due to the Ge alloying. Fig. 3 shows thermoelectric transport properties of  $\text{Mg}_2\text{Sn}_{1-x-y}\text{Ge}_x\text{Sb}_y$  as a function of Ge content at room temperature.  $PF$  at room temperature of  $\text{Mg}_2\text{Sn}_{1-x-y}\text{Ge}_x\text{Sb}_y$  significantly increased with Ge content from  $x = 0.05$  to  $0.25$ , and reached a peak value of  $45 \mu\text{W cm}^{-1} \text{K}^{-2}$  at  $x = 0.25$ , then decreased as Ge content was further increased to  $x = 0.3$ , as shown in the Fig. 3 (a). Hall measurement was conducted to understand the mechanism lying behind. Here, both the Hall coefficient ( $R_H$ ) and Hall factor ( $r_H$ ) is used to calculate the real carrier concentration (see details in ESI†).<sup>32, 40</sup>

Considering the real carrier concentration, we split the  $PF$  ( $S^2\sigma$ ) into  $S^2n$  and  $\mu$ , as shown in the Fig. 3 (b, c). Like  $PF$ ,  $S^2n$  increases with Ge content from  $x = 0.05$  to  $0.25$ , then decreases. On the other hand, we observed a decrease of  $\mu$  with increasing Ge in the whole range. In other words, the improved  $PF$ , due to the Ge alloying effect, is resulted from the enhanced  $S^2n$  which is mainly determined by the effective carrier mass at a given Fermi energy. Fig. 3 (d) plots the calculated carrier effective mass of  $\text{Mg}_2\text{Sn}_{1-x-y}\text{Ge}_x\text{Sb}_y$  as a function of the Ge content. Although we have varying content of Sb and extra Mg,  $m^*$  of  $\text{Mg}_2\text{Sn}_{1-x-y}\text{Ge}_x\text{Sb}_y$  increases linearly with increasing Ge content from  $x = 0$  to  $0.2$ , and reaches a peak value  $m^* = 3.5 m_0$  at  $x = 0.25$ , and then slightly decreases for the sample with  $x = 0.3$ . The change of  $m^*$  could be understood through the contribution of the additional band above the bottom of conduction band. Since the significant enhancement of  $m^*$ , the parameter  $U^*$  (defined in Eq. (3)) also appears in similar behavior with Ge content, as shown Fig. 3 (e). Fig. 3 (f) shows the composition dependent band structure evaluation in the  $\text{Mg}_2\text{Sn}_{1-x}\text{Ge}_x$  system, according to the early work<sup>28, 29</sup>. Here, the  $E_A$  is the edge difference between two sub-bands in the conduction band. For  $\text{Mg}_2\text{Sn}$ , the additional band is about  $0.16 \text{ eV}$  higher than the main band. Since  $E_A > 5k_B T$ , the

contribution of additional band to the total electronic transport is negligible near room temperature.<sup>10</sup> However,  $E_d$  changes as Ge gets into Sn-site to form an alloy of  $\text{Mg}_2\text{Sn}_{1-x}\text{Ge}_x$ . The decreasing  $E_d$  with Ge content in the  $\text{Mg}_2\text{Sn}_{1-x}\text{Ge}_x$  significantly raises the contribution of the additional band to the electronic transport. Furthermore, a band crossing is predicted around Ge content of  $x = 0.22$  in  $\text{Mg}_2\text{Sn}_{1-x}\text{Ge}_x$  according to Zaitsev *et al.*'s work.<sup>28, 29</sup> First-principles calculation was conducted to understand the mechanism behind the band convergence between the two sub-bands near the conduction band edge in  $\text{Mg}_2\text{X}$  ( $X = \text{Sn, Ge}$ ) system. Fig. 4 shows the band structure and total DOS for  $\text{Mg}_2\text{Sn}$  and  $\text{Mg}_2\text{Ge}$ . It is clearly shown that both  $\text{Mg}_2\text{Sn}$  and  $\text{Mg}_2\text{Ge}$  have valance-band top at  $\Gamma$ -point and a conduction-band bottom at the X-point, which is consistent with the recently reported calculations.<sup>41, 42</sup> Furthermore, two sub-bands at the conduction band edges were observed in both compounds, but the position at X point was switched. Here, among these two sub-bands at X-point of  $\text{Mg}_2\text{Sn}$ , the bottom one is referred as  $X_H$ -band (red color) while the above one is referred as the  $X_L$ -band (blue color). The calculated  $E_d$  between  $X_H$ -band and  $X_L$ -band at X point is around 0.27 eV. The position switching of  $X_H$ -band and  $X_L$ -band at X-point from  $\text{Mg}_2\text{Sn}$  to  $\text{Mg}_2\text{Ge}$  confirmed the band convergence effect in  $\text{Mg}_2\text{Sn}_{1-x}\text{Ge}_x$ .

Fig. 5 shows the projected DOS for Mg: s, Mg: p, Sn: s, Sn: p, Sn: d- $e_g$  and Sn: d- $t_{2g}$  orbitals for  $\text{Mg}_2\text{Sn}$ , and Mg: s, Mg: p, Ge: s, Ge: p, Ge: d- $e_g$  and Ge: d- $t_{2g}$  orbitals for the  $\text{Mg}_2\text{Ge}$ . At the first glance,  $\text{Mg}_2\text{Sn}$  has the conduction band mainly composed of unoccupied Mg: 3s orbital ( $X_H$ -band) followed by the unoccupied Mg: 3p-Sn: 6s hybridized orbital ( $X_L$ -band), while  $\text{Mg}_2\text{Ge}$  has the conduction band mainly consisting of unoccupied Mg: 3p-Ge: 5s hybridized orbital ( $X_L$ -band) followed by the Mg: 3s orbital ( $X_H$ -band) as shown in the Fig. 5 (a, b, e, f). In order to get more details, the value of  $d(\text{p-DOS})/dE$  versus energy was plotted in the Fig. 5 (c, g) for  $\text{Mg}_2\text{Sn}$  and  $\text{Mg}_2\text{Ge}$ , respectively. We found that the unoccupied Sn: 5d orbital in  $\text{Mg}_2\text{Sn}$  and Ge: 4d orbital in  $\text{Mg}_2\text{Ge}$  are split due to the hexahedral crystalline field into twice-degenerated d- $e_g$  orbital and triple-degenerated d- $t_{2g}$ . Furthermore, in  $\text{Mg}_2\text{Sn}$ , both the  $d(\text{p-DOS})/dE$  of Sn: d- $t_{2g}$  and Mg: 3s orbital show a peak at the energy of the 0.27 eV, while the  $d(\text{p-DOS})/dE$  of

Sn: d- $e_g$ , Mg: 3p and Sn: 6s shows a peak at an energy of 0.6 eV, as shown in Fig. 5 (c, d). Similar coincidence was also observed in the  $\text{Mg}_2\text{Ge}$ , as shown in Fig. 5 (g, h). These results suggested a new scenario for the conduction band formation of  $\text{Mg}_2\text{Sn}$  and  $\text{Mg}_2\text{Ge}$ . In the  $\text{Mg}_2\text{X}$  ( $X = \text{Sn, Ge}$ ),  $X_H$ -band is formed by the hybridized Mg: 3s and Sn: 5d- $t_{2g}$ /Ge:4d- $t_{2g}$  orbitals while  $X_L$ -band results from the hybridized Mg: 3p, Sn 6s, and Sn: 5d- $e_g$ /Ge: 4d- $e_g$  orbitals. The change of the ionic size  $r^+/r^-$  ratio could be the most likely reason for the composition band crossing in the  $\text{Mg}_2\text{Sn}_{1-x}\text{Ge}_x$  systems. The increased carrier effective mass due to the band crossing is finally responsible for the significant enhancement of the weighted mobility  $U$ .

### 4.3 Decreased bipolar thermal conductivity due to increased $E_g$

Bipolar effect owing to the intrinsic carrier excitation has a deleterious influence on the thermoelectric performance of materials, which adds a new term in the total thermal conductivity to significantly reduce  $ZT$  at high temperature. The thermal conductivity due to the bipolar effect is given by the following,<sup>5, 11</sup>

$$\kappa_{\text{bipolar}} = -\frac{\sigma_e \sigma_h}{\sigma_e + \sigma_h} (S_e - S_h)^2 T \quad (14)$$

where  $\sigma_e$ ,  $\sigma_h$ ,  $S_e$ , and  $S_h$  are the electron conductivity, hole conductivity, electron Seebeck coefficient, and hole Seebeck coefficient, respectively. Conventionally, widening of band gap  $E_g$  significantly suppresses the intrinsic excitation, reduces minor carrier, and hence the  $\kappa_{\text{bipolar}}$ .

Fig. 6 (a, b) shows the estimated bipolar thermal conductivities of  $\text{Mg}_2\text{Sn}_{1-x}\text{Ge}_x\text{Sb}_y$ . The detailed numerical calculation about the bipolar thermal conductivity is shown in the ESI†. It is found that adding Ge obviously reduces  $\kappa_{\text{bipolar}}$ .

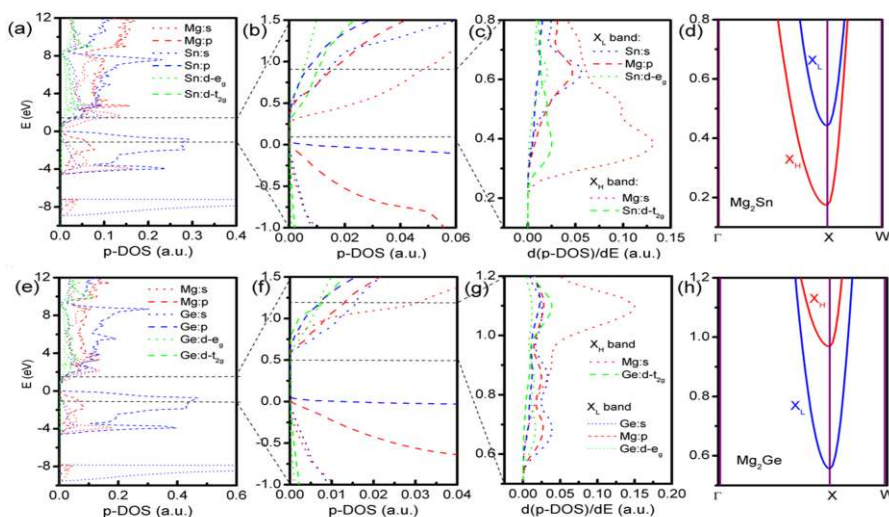


**Fig. 5.** Projected density of states (DOS) for  $\text{Mg}_2\text{Sn}$  (a-d) and  $\text{Mg}_2\text{Ge}$  (e-h). (a, b, e, and f) Energy versus p-DOS, (c, g) Energy versus  $d(\text{p-DOS})/dE$ , (d, h) band structure.

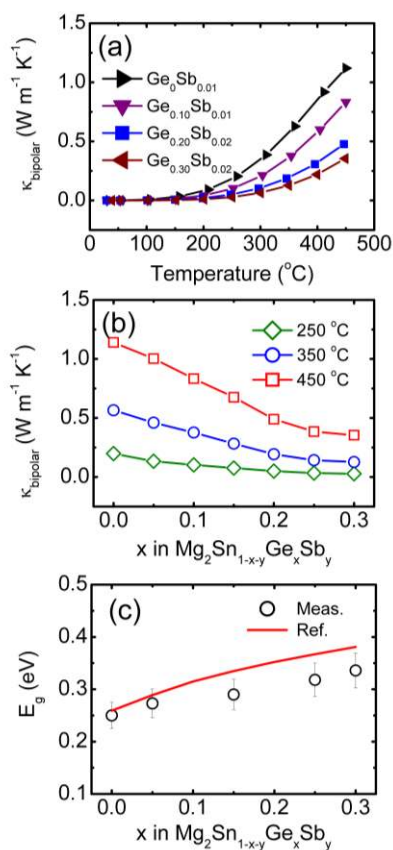


**Fig. 6.** Calculated bipolar thermal conductivity of  $\text{Mg}_2\text{Sn}_{1-x-y}\text{Ge}_x\text{Sb}_y$  as a function of (a) temperature and (b) Ge content, (c) band gap of  $\text{Mg}_2\text{Sn}_{1-x-y}\text{Ge}_x\text{Sb}_y$  derived from the absorption edge. The reference data in figure (c) was from the Ref. 28.

As an example, the bipolar thermal conductivity at 450 °C is  $0.2 \text{ W m}^{-1} \text{ K}^{-1}$  for  $\text{Mg}_2\text{Sn}_{0.728}\text{Ge}_{0.25}\text{Sb}_{0.022}$ , but  $1.2 \text{ W m}^{-1} \text{ K}^{-1}$  for  $\text{Mg}_2\text{Sn}_{0.99}\text{Sb}_{0.01}$ . The significant suppression of  $\kappa_{\text{bipolar}}$  shifts the peak  $ZT$  of  $\text{Mg}_2\text{Sn}_{1-x}\text{Ge}_x\text{Sb}_y$  towards higher temperature. In order to investigate the effect of Ge content on the band gap in  $\text{Mg}_2\text{Sn}_{1-x}\text{Ge}_x\text{Sb}_y$ , the Fourier transform infrared spectrum of selected samples were measured to derive the optical band gap. For near-normal incidence, the complex refractive index  $n(\omega)$  and the extinction coefficient  $k(\omega)$  with both the real and imaginary parts can be obtained from the Kramers-Kronig analysis (see details in ESI†).<sup>44, 45</sup> Fig. 6 (c) plots the measured band gap of  $\text{Mg}_2\text{Sn}_{1-x}\text{Ge}_x\text{Sb}_y$  as a function of Ge content. It shows a linear increase from  $E_g = 0.25 \text{ eV}$  to  $0.34 \text{ eV}$  with increasing Ge content from  $x = 0$  to  $0.3$ . At a given Ge content, our measured band gap is slightly smaller than the values obtained in the early work in  $\text{Mg}_2\text{Sn}_{1-x}\text{Ge}_x$ ,<sup>28, 29</sup> which could be due to the heavy doping level of Sb dopant. Additionally, there is an absorption band in the lower energy range in  $\text{Mg}_2\text{Sn}_{1-x}\text{Ge}_x\text{Sb}_y$  with Ge content  $x \geq 0.1$ . As an example, such absorption band is centered at  $0.17 \text{ eV}$  (Fig. S5, ESI†), which may be related to the electronic transition between multiple conduction bands.<sup>45, 46</sup> Furthermore, from our new viewpoint suggested by Eq. (10), the widening band gap contributes to the enhancement in the new material parameter  $B^*$  and hence increase of maximum  $ZT$  with respect to doping concentration and temperature.

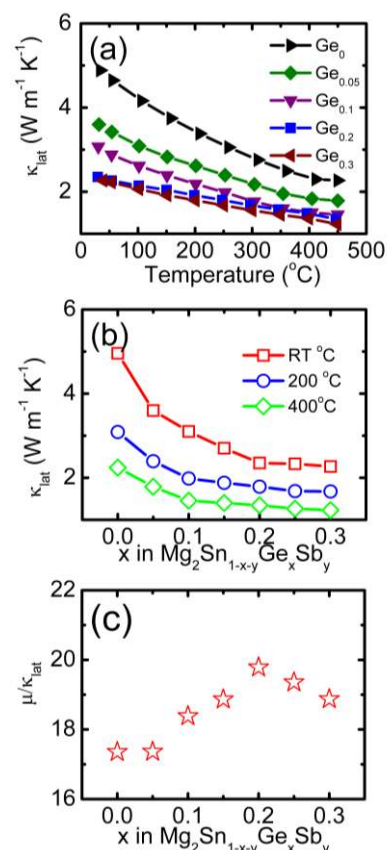


**Fig. 7.** Calculated lattice thermal conductivity of  $\text{Mg}_2\text{Sn}_{1-x-y}\text{Ge}_x\text{Sb}_y$  as a function of (a) temperature and (b) Ge content, and (c)  $\mu/\kappa_{\text{lat}}$  of  $\text{Mg}_2\text{Sn}_{1-x-y}\text{Ge}_x\text{Sb}_y$  as function of Ge content. The unit is  $\text{cm}^2 \text{ V}^{-1} \text{ s}^{-1}$  for  $\mu$ ,  $\text{W m}^{-1} \text{ K}^{-1}$  for  $\kappa_{\text{lat}}$ .

In the case of  $\text{Mg}_2\text{Sn}_{1-x}\text{Ge}_x\text{Sb}_y$ , the  $E_g$  of  $\text{Mg}_2\text{Sn}_{0.73}\text{Ge}_{0.25}\text{Sb}_{0.02}$  ( $E_g = 0.318 \text{ eV}$ ) is 27% higher than that of  $\text{Mg}_2\text{Sn}_{0.99}\text{Sb}_{0.01}$  ( $E_g = 0.250 \text{ eV}$ ), which partially contributes to the enhancement in  $B^*$  from 0.85 to 2.73, as shown in Table S1. The different  $B^*$  make materials corresponding maximum  $ZT$  occur at different optimized doping concentration and temperature.

#### 4.4 Decreased lattice thermal conductivity due to alloying effect

Fig. 7 (a, b) shows the lattice thermal conductivity ( $\kappa_{\text{lat}}$ ) dependence on temperature and Ge content in  $\text{Mg}_2\text{Sn}_{1-x-y}\text{Ge}_x\text{Sb}_y$ , respectively. Here, the  $\kappa_{\text{lat}}$  was estimated by subtracting the parts contributed by both the charge carriers ( $\kappa_{\text{carr}}$ ) and  $\kappa_{\text{bipolar}}$ . The details about the numerical calculation were provided in the ESI†. The  $\kappa_{\text{lat}}$  at room temperature of  $\text{Mg}_2\text{Sn}_{1-x-y}\text{Ge}_x\text{Sb}_y$  is 4.96, 3.59, 3.10, 2.70, 2.35, 2.33, and  $2.27 \text{ W m}^{-1} \text{ K}^{-1}$  for  $x = 0, 0.05, 0.10, 0.15, 0.20, 0.25,$  and  $0.30$ , respectively. The continuous decrease in  $\kappa_{\text{lat}}$  with increasing Ge content demonstrates a strong alloying scattering to phonon transport because of the mass difference between Ge and Sn. It is noted that similar decrease in  $\mu$  with increasing Ge was shown before. Fig. 7 (c) plots the ratio of  $\mu$  (unit:  $\text{cm}^2 \text{ V}^{-1} \text{ s}^{-1}$ ) to  $\kappa_{\text{lat}}$  (unit:  $\text{W m}^{-1} \text{ K}^{-1}$ ) as a function of Ge content in  $\text{Mg}_2\text{Sn}_{1-x-y}\text{Ge}_x\text{Sb}_y$ . It shows an increased  $\mu/\kappa_{\text{lat}}$  ratio with increasing Ge content from  $x = 0$  to  $0.2$ , and then a decreased  $\mu/\kappa_{\text{lat}}$  ratio with  $x > 0.2$ .



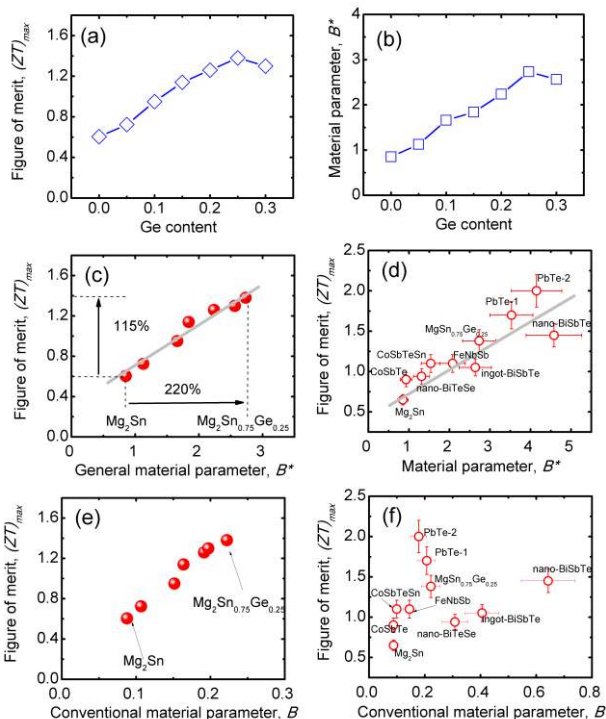


**Fig. 8.** (a) Ge content dependent peak  $(ZT)_{max}$  for  $Mg_2Sn_{1-x-y}Ge_xSb_y$ , (b) Ge content dependent material parameter  $B^*$  for  $Mg_2Sn_{1-x-y}Ge_xSb_y$ , (c)  $(ZT)_{max}$  versus  $B^*$  for  $Mg_2Sn_{1-x-y}Ge_xSb_y$ , (d)  $(ZT)_{max}$  versus  $B^*$  for reported materials. (e)  $(ZT)_{max}$  versus conventional  $B$  for  $Mg_2Sn_{1-x-y}Ge_xSb_y$ , (d)  $(ZT)_{max}$  versus conventional  $B$  for reported materials.

#### 4.5 Relationship between $B^*$ and $ZT$

With the fundamental parameters  $U^*$ ,  $\kappa_{lat}$ , and  $E_g$  examined, here we show how the  $ZT$  enhancement can be understood as a synergistic effect combining all the benefits in regards to the generalized material parameter  $B^*$ . Fig. 8 (a) plots the peak  $(ZT)_{max}$  of  $Mg_2Sn_{1-x-y}Ge_xSb_y$  as a function of Ge content. It shows a peak value around the Ge content of  $x = 0.25$ . In order to explore the connection between  $ZT$  and the fundamental parameter  $B^*$ , defined in Eq. (11),  $B^*$  is calculated using  $U^*$  and  $E_g$  at room temperature and  $\kappa_{lat}$  at temperature corresponding to peak  $(ZT)_{max}$ , as shown in Fig. 8 (b). The calculated  $B^*$  shows a continuous increase from 0.85 to 2.73 with increasing Ge content from  $x = 0$  to 0.25. Such an enhancement in  $B^*$  is contributed by ~25% enhancement in weighted mobility  $U^*$ , ~27% increase in  $E_g$ , and ~50 % decrease in  $\kappa_{lat}$ . As compared with  $x = 0.25$ , the sample with Ge of  $x = 0.3$  has smaller  $B^*$  of 2.56 due to a smaller  $U^*$ . The Ge content dependent behavior of  $B^*$  is quite similar to that of  $ZT$ . Fig. 8 (c) plots peak  $(ZT)_{max}$  of  $Mg_2Sn_{1-x-y}Ge_xSb_y$  as a function of their corresponding  $B^*$ , where it is seen that higher  $B^*$  corresponds to a higher  $(ZT)_{max}$ . In order to further confirm the connection between the  $(ZT)_{max}$  and  $B^*$ ,  $(ZT)_{max}$  of selected materials, including  $CoSb_3$ ,<sup>43, 47</sup>  $Bi_2Te_3$ ,<sup>48,49</sup>  $PbTe$ ,<sup>50-51</sup> and  $FeNbSb$ <sup>52</sup> was plot as a function of their estimated  $B^*$  in Fig. 8 (d). The detailed estimated  $U^*$ ,  $E_g$ , and  $\kappa_{lat}$  are summarized in Table S1 (ESI†). It is noted that the reported  $(ZT)_{max}$  could be either lower or higher than theoretical  $(ZT)_{max}$  with optimized  $(\zeta_f, \zeta_g)$  (or  $(N_D, T)$ ) according to Eq. (10), because of the limited investigated dopant points or the measurement error. A 10% error bar is

therefore added in the  $(ZT)_{max}$ . On the other hand, the estimated  $B^*$  could be less accurate since we do not have the measured  $m^*$  and  $\mu$  for  $U^*$ , and measured  $E_g$ . In this case, the term of  $\mu (m^*)^{3/2}$  is estimated from the measured  $\sigma$  and  $S$ , while  $E_g$  is estimated using formula  $E_g = 2eS_{max}T$ .<sup>53</sup> A 15% error bar is therefore added in  $B^*$ . A similar conclusion that a higher  $B^*$  leads to a higher  $(ZT)_{max}$  is seen in Fig. 8 (d). For comparison, the  $(ZT)_{max}$  versus conventional material parameter  $B$  was shown in Fig. 8(e, f). Here,  $T=300K$  was used to estimate the  $B$  according to Eq. (1). Fig. 8(e) suggested that the conventional material parameter  $B$  was still a good guidance for  $Mg_2Sn_{1-x-y}Ge_xSb_y$ , but not good enough for other materials. It is therefore reasonable to consider the generalized material parameter  $B^*$  as a new fundamental parameter for exploring better thermoelectric materials, which is directly proportion to  $U^*$  and  $E_g$ , while inversely proportional to  $\kappa_{lat}$ . Eq. (12) suggests that widening of  $E_g$  could have equivalent importance as increased  $U^*$  and decreased  $\kappa_{lat}$ . Recently, Zhao *et al.* reported a high  $ZT_{max}$  of 2.0 in  $PbTe$  with 6% $MgTe$ . One of the favorable effects from  $MgTe$  is the suppressed bipolar thermal conductivity due to the widening of band gap as compared with pure  $PbTe$ . The material parameter  $B^*$  for  $PbTe$ : 6% $MgTe$  was calculated and included in Fig. 8 (d), which also follows the trend. It is noted that the error bar of  $B^*$  for  $PbTe$  may be even bigger due to the temperature dependent  $m^*$  and  $E_g$ . Besides of the alloying effect for widening  $E_g$ , the carrier filtering effect due to the grain boundary could have a similar band gap widening effect. For example,  $E_g$  of nano- $BiSbTe$  (0.184 eV) is slightly larger than that of ingot- $BiSbTe$  (0.167 eV), which is consistent with the reported notable reduction in the bipolar thermal conductivity in nano- $BiSbTe$ .<sup>48</sup> The grain boundary scattering is also responsible the significant decrease in  $\kappa_{lat}$  from ingot- $BiSbTe$  (0.88  $W m^{-1} K^{-1}$ ) to nano- $BiSbTe$  (0.52  $W m^{-1} K^{-1}$ ). However, in most cases, the grain boundary has notorious effect on the carrier mobility, compromising the benefit from the widening band gap and decreased lattice thermal conductivity. A selective scattering mechanism for the carriers is desired for such kind of carrier filtering grain boundaries. Similar selective carrier filtering effect was noted in half-Heusler materials.<sup>54</sup> As we pointed out, increasing  $U^*$ , reducing  $\kappa_{lat}$ , or widening  $E_g$  can be achieved readily. However, it is challenging to synergistically achieve all of them.  $Mg_2Sn_{1-x-y}Ge_xSb_y$  is one good example, which shows a simultaneous ~25% enhancement in  $U^*$ , ~27% increase in  $E_g$ , and ~50 % decrease in  $\kappa_{lat}$  by tuning the Ge content, boosting the  $ZT$  from 0.6 for  $Mg_2Sn_{0.99}Sb_{0.01}$  to 1.4 for  $Mg_2Sn_{0.73}Ge_{0.25}Sb_{0.02}$ . The new material parameter  $B^*$  opens opportunities to further boost the performance of existing materials, and to discover new materials by quantitatively identifying the roles of the fundamental parameters  $U^*$ ,  $E_g$  and  $\kappa_{lat}$  that affects the thermoelectric performance. It is worthy to point out that the components ( $U^*$ ,  $E_g$ , and  $\kappa_{lat}$ ) among the material parameter  $B^*$  are still interconnected with each other from more fundamental point of view. In the ESI†, we show a simply discussion about the relation between  $U^*$  and  $E_g$  based on k-p perturbation theory,<sup>55</sup> and explain why most thermoelectric materials have narrow instead of wide band gap. Further explorations into the relation among the parameters in generalized material parameter  $B^*$ , would be more insightful to guide the researcher to atomically construct ideal materials with optimized atomic sizes, bonding strengths, and crystalline structures.

#### 5 Conclusion

In summary, the significant enhancement in the  $ZT$  values of  $Mg_2Sn_{1-x-y}Ge_xSb_y$  from 0.6 at  $x = 0$  to 1.4 at  $x = 0.25$  was understood through a generalized material parameter  $B^*$ , proposed to be applicable over a wider temperature range, especially taking into account the bipolar effect at high temperatures. This generalized material parameter connects the weighted mobility, lattice thermal conductivity, and the band gap, to characterize material's thermoelectric performance in the two-dimensional (doping level and temperature) parameter space. It is found that the Ge alloying approach leads to a ~25% enhancement in weighted mobility  $U^*$ , ~27% increase in  $E_g$ , and ~50 % decrease in  $\kappa_{lat}$ , which resulted in ~220% increase in the material parameter  $B^*$ . The increased weighted mobility corresponds to a significant enhancement in  $PF$ . The band gap widening leads to an appreciable suppression of the bipolar thermal conductivity.  $Mg_2Sn_{1-x-y}Ge_xSb_y$  presents a good example to simultaneously tune the three fundamental parameters  $U^*$ ,  $\kappa_{lat}$  and  $E_g$ . By using the generalized material parameter  $B^*$ , the fundamental parameters ( $U^*$ ,  $\kappa_{lat}$  and  $E_g$ ) can be evaluated on the same footing, which we believe will help to better identify new thermoelectric material systems in the future.

## Acknowledgement

The authors would like to thank Dr. David. J Singh at Oak Ridge National Laboratory for the helpful advice in the first principle calculation. This work is supported by "Solid State Solar-Thermal Energy Conversion Center (S<sup>3</sup>TEC)", an Energy Frontier Research Center funded by the U.S. Department of Energy, Office of Science, Office of Basic Energy Science under award number DE-SC0001299/DE-FG02-09ER46577. J.M.B acknowledges support from National Science Foundation (Career Award ECCS-1240510) and the Robert A. Welch Foundation (E-1728)".

<sup>a</sup> Department of Physics and TcSUH, University of Houston, Houston, Texas 77204, USA. Fax: 713-743-8201; Tel: 713-743-8227;

<sup>b</sup> Department of Mechanical Engineering, Massachusetts Institute of Technology, Cambridge, Massachusetts 02139, USA. Fax: 1-617-324-5519; Tel: 1-617-253-0006;

<sup>c</sup> Department of Electrical and Computer Engineering, University of Houston, Houston, Texas 77204, USA

\* To whom correspondence should be addressed: [gchen2@mit.edu](mailto:gchen2@mit.edu); [zren@uh.edu](mailto:zren@uh.edu)

## References

1. A. F. Ioffe, *Semiconductor thermoelements, and thermoelectric cooling*, Infosearch, London, 1957.
2. C. M. Bhandari, D. M. Rowe, *Optimization of carrier concentration*, in book: *CRC handbook of thermoelectric*, edited by D. M. Rowe, CRC Press, Boca Raton, 1995.
3. W. S. Liu, X. Yan, G. Chen and Z. F. Ren, *Nano Energy*, 2012, **1**, 42-56.
4. R. P. Chasmar and R. Stratton, *J. Electron. Control*, 1959, **7**, 52-72.
5. H. J. Goldsmid, *British J. Appl. Phys.*, 1960, **11**, 209-217.
6. D. Tuomi, *J. Electrochem. Soc.*, 1984, **131**, 2101-2105.
7. G. D. Mahan, *Solid State Physics*, 1997, **51**, 81-157.
8. G. S. Nolas, J. Sharp and H. J. Goldsmid, *Thermoelectrics basic principles and new materials developments*, Springer-Verlag, Berlin Heidelberg, 2001.
9. H. Wang, Y. Z. Pei, A. D. LaLonde and G. J. Snyder, *Material design considerations based on thermoelectric quality factor*,

in book: *Thermoelectric nanomaterials*, Springer Series in Materials Science 182, edited by K. Koumoto and T. Mori , DOI: 10.1007/978-3-642-37537-8\_1, Springer-Verlag, Berlin Heidelberg, 2013.

10. W. S. Liu, L. D. Zhao, B. P. Zhang, H. L. Zhang and J. F. Li, *Appl. Phys. Lett.* , 2008, **93**, 042109-3.
11. R. Simon, *J. Appl. Phys.*, 1962, **33**, 1830-1841.
12. C. Wood, *Rep. Prog. Phys.*, 1988, **51**, 459.
13. G. D. Mahan, *J. Appl. Phys.*, 1989, **65**, 1578-1583.
14. J. O. Sofo and G. D. Mahan, *Phys. Rev. B*, 1994, **49**, 4565-4570.
15. J. F. Li, W. S. Liu, L. D. Zhao and M. Zhou, *NPG Asia Mater.*, 2010, **2**, 152-158 .
16. C. J. Vineis, A. Shakouri, A. Majumdar and M. G. Kanatzidis, *Adv. Mater.*, 2010, **22**, 3970-3980.
17. B. Qiu, Z. T. Tian, A. Vallabhaneni, B. L. Liao, J. M. Mendoza, O. D. Restrepo, X. L. Ruan and G. Chen, *Europhys. Lett.*, 2015, **109**, 57006-6.
18. M. Zebarjadi, G. Joshi, G. H. Zhu, B. Yu, A. Minnich, Y. C. Lan, X. W. Wang, M. Dresselhaus, Z. F. Ren and G. Chen, *Nano Lett.*, 2011, **11**, 2225-2230.
19. Y. Xiao, G. Joshi, W. S. Liu, Y. C. Lan, H. Wang, S. Y. Lee, J. W. Simonson, S. J. Poon, T. M. Tritt, G. Chen, and Z. F. Ren, *Nano Lett.*, 2011, **11**, 556-560.
20. L. D. Zhao, J. Q. He, S. Q. Hao, C. I. Wu, T. P. Hogan, C. Wolverton, V. P. Dravid and M. G. Kanatzidis, *J. Am. Chem. Soc.*, 2012, **134**, 16327-16336.
21. J. P. Heremans, V. Jovovic, E. S. Toberer, A. Saramat, K. Kurosaki, A. Charoenphakdee, S. Yamanaka and G. J. Snyder, *Science*, 2008, **321**, 554-557.
22. Q. Y. Zhang, H. Wang, W. S. Liu, H. Z. Wang, B. Yu, Q. Zhang, Z. T. Tian, G. Ni, S. Y. Lee, K. Esfarjani, G. Chen and Z. F. Ren, *Energy Environ. Sci.*, 2012, **5**, 5246-5251.
23. Q. Zhang, B. L. Liao, Y. C. Lan, K. Lukas, W. S. Liu, K. Esfarjani, C. P. Opeil, D. Broido, G. Chen, and Z. F. Ren, *Proc. Nat. Acad. Sci. USA*, 2013, **110**, 13261-13266.
24. Y. Z. Pei, X. Y. Shi, A. LaLonde, H. Wang, L. D. Chen and G. J. Snyder, *Nature*, 2011, **473**, 66-69.
25. W. Liu, X. J. Tian, K. Yin, H. J. Liu, X. F. Tang, J. Shi, Q. J. Zhang and C. Uher, *Phys. Rev. Lett.*, 2012, **108**, 166601-5.
26. D. M. Rowe and C. M. Bhandari, *Modern thermoelectrics*, Reston Publishing Company, Reston Virginia, 1983.
27. Z. T. Tian, J. Garg, K. Esfarjani, T. Shiga, J. Shimoni and G. Chen, *Phys. Rev. B*, 2012, **85**, 184303-7.
28. V. K. Zaitsev, M. I. Fedorov, I. S. Eremin and E. A. Gurieva, Thermoelectrics on the base of solid solutions of Mg<sub>2</sub>BIV compounds (BIV=Si, Ge, Sn), in book: *Thermoelectric handbook: macro to nano structure materials*, CRC Press, New York, 2005.
29. V. K. Zaitsev, M. I. Fedorov, E. A. Gurieva, I. S. Eremin, P. P. Konstantinov, A. Yu. Samunin and M. V. Vedernikov, *Phys. Rev. B*, 2006, **74**, 045207-5.
30. R. B. Song, T. Aizawa and J. Q. Sun, *Mater. Sci. Eng. B*, 2006, **136**, 111-117.
31. Q. Zhang, J. He, X. B. Zhao, S. N. Zhang, T. J. Zhu, H. Yin and T. M. Tritt, *J. Phys. D.*, 2008, **41**, 185103-6.
32. X. H. Liu, T. J. Zhu, H. Wang, L. P. Hu, H. H. Xie, G. Y. Jiang, G. J. Snyder and X. B. Zhao, *Adv. Energy Mater.* , 2013, **3**, 1238-1244.
33. A. U. Khan, N. V. Vlachos, E. Hatzikraniotis, G. S. Polymeris, Ch. B. Lioutas, E. C. Stefanaki, K. M. Paraskevopoulos, I. Giapintzakis and Th. Kyratsi, *Acta Mater.*, 2014, **77**, 43-53.
34. L. B. Zhang, P. H. Xiao, L. Shi, G. Henkelman, J. B. Goodenough and J. S. Zhou, *J. Appl. Phys.*, 2015, **117**, 155103.
35. W. S. Liu, H. S. Kim, S. Chen, Q. Jie, B. Lv, M. L. Yao, Z. S. Ren, C. P. Opeil, S. Wilson, C. W. Chu and Z. F. Ren, *Proc. National. Acad. Sci. USA*, 2015, **112**, 3269-3274.
36. D. J. Singh and L. Nordstrom. *Planewaves, pseudopotentials and the LAPW method*, 2<sup>nd</sup> ed. Springer-Verlag, Berlin Heidelberg, 2006.

- 
37. P. Blaha, K. Sshwarz, G. K. H. Madsen, D. Kvasnicka and J. Luitz, WIEN2K: An augmented plane wave plus local orbital program for calculating crystal properties, 2001.
38. J. P. Perdew, K. Burke and M. Ernzerhof, *Phys. Rev. Lett.*, 1996, **77**, 3865-3868.
39. F. Tran and P. Blaha, *Phys. Rev. Lett.*, 2009, **102**, 226401-4.
40. H. J. Goldsmid, *Applications of Thermoelectricity*, Butler & Tanner, London 1960.
41. J. J. Pulikkotil, D. J. Singh, S. Auluck, M. Saravanan, D. K. Misra, A. Dhar and R. C. Budhani, *Phys. Rev. B*, 2012, **86**, 155204-8.
42. K. Kutorasinski, B. Wiendlocha, J. Tobola and S. Kaprzyk, *Phys. Rev. B*, 2014, **89**, 115205-8.
43. W. S. Liu, B. P. Zhang, J. F. Li, H. L. Zhang and L. D. Zhao, *J. Appl. Phys.*, 2007, **102**, 103717-7.
44. D. M. Roessler, *British J. Appl. Phys.*, 1965, 16, 1119-1123.
45. W. J. Scouler, *Phys. Rev.*, 1969, **178**, 1353-1357.
46. H. G. Lipson and A. Kahan, *Phys. Rev.*, 1964, **133**, A800-A810.
47. W.S. Liu, B. P. Zhang, L. D. Zhao and J. F. Li, *Chem. Mater.* 2008, **20**, 7526-7531.
48. B. Poudel, Q. Hao, Y. Ma, Y. C. Lan, A. Minnich, B. Yu, X. Yan, D. Z. Wang, A. Muto, D. Vashaee, X. Y. Chen, J. M. Liu, M. S. Dresselhaus, G. Chen and Z. F. Ren, *Science*, 2008, 3420, 634-638.
49. W. S. Liu, Q. Y. Zhang, Y. C. Lan, S. Chen, X. Yan, Q. Zhang, H. Wang, D. Z. Wang, G. Chen and Z. F. Ren, *Adv. Energy Mater.*, 2011, **1**, 577-587.
50. Q. Y. Zhang, H. Z. Wang, Q. Zhang, W. S. Liu, B. Yu, H. Wang, D. Z. Wang, G. Ni, G. Chen and Z. F. Ren, *Nano Lett.* 2012, **12**, 2324-2330.
51. L. D. Zhao, H. J. Wu, S. Q. Hao, C. I. Wu, X. Y. Zhou, K. Biswas, J. Q. He, T. P. Hogan, C. Uher, C. Wolverton, V. P. Dravid, and M. G. Kanatzidis, *Energy Environ. Sci.* 2013, **6**, 3346-3355.
52. C. G. Fu, T. J. Zhu, Y. T. Liu, H. H. Xie, and X. B. Zhao, *Energy Environ. Sci.* 2015, **8**, 216-220.
53. H. J. Goldsmid, and J. W. Sharp, *J. Electron. Mater.* 1999, **28**, 869-872.
54. W. S. Liu, Z. F. Ren and G. Chen, *Nanostructured thermoelectric materials*, in book: *Thermoelectric nanomaterials*, Springer Series in Materials Science 182 ,edited by K. Koumoto and T. Mori , DOI: 10.1007/978-3-642-37537-8\_1, Springer-Verlag, Berlin Heidelberg, 2013.
55. P. Y. Yu, and M. Cardona, *Fundamentals of semiconductors: Physics and Materials properties*, Springer-Verlag, Berlin Heidelberg, 2010.

Supporting Information for:

## New insight into the material parameter $B$ to understand the enhanced thermoelectric performance of $\text{Mg}_2\text{Sn}_{1-x-y}\text{Ge}_x\text{Sb}_y$

5 Weishu Liu<sup>1</sup>, Jiawei Zhou<sup>2</sup>, Qing Jie<sup>1</sup>, Yang Li<sup>3</sup>, Hee Seok Kim<sup>1</sup>, Jiming Bao<sup>3</sup>, Gang Chen<sup>2\*</sup>, and Zhifeng Ren<sup>1\*</sup>

<sup>1</sup>Department of Physics and TcSUH, University of Houston, Houston, Texas 77204, USA

<sup>2</sup>Department of Mechanical Engineering, Massachusetts Institute of Technology, Cambridge, Massachusetts 02139, USA

<sup>3</sup>Department of Electrical and Computer Engineering, University of Houston, Houston, Texas 77204, USA

\* To whom correspondence should be addressed: [gchen2@mit.edu](mailto:gchen2@mit.edu), [zren@uh.edu](mailto:zren@uh.edu)

10

15

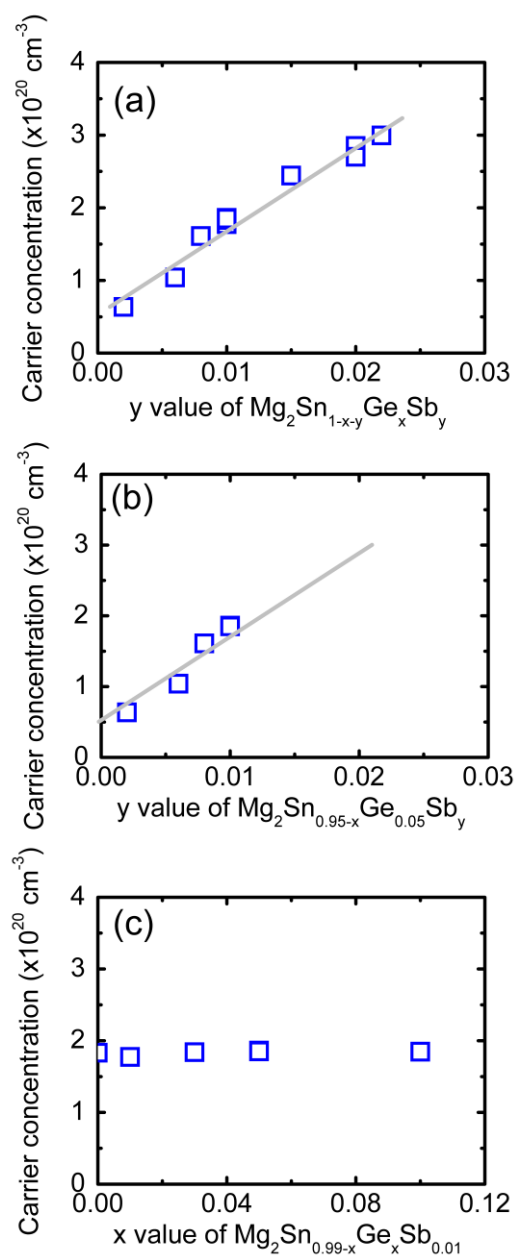
20

Table S1 Physical property of selected thermoelectric materials.

Short name	Composition	$(ZT)_{\text{max}}$	$m^*$	$U^*$	$\kappa_{\text{lat}}$	$E_{\text{g}}$	$B^*$	Ref.
		[/]	[ $m_0$ ]	[ $\text{m K}^{-3/2} \text{s}^{-1} \text{V}^{-1}$ ]	[ $\text{W m}^{-1} \text{K}^{-1}$ ]	[eV]	[/]	
$\text{Mg}_2\text{Sn}$	$\text{Mg}_2\text{Sn}_{0.99}\text{Sb}_{0.01}$	0.65, 350 °C	2.04	130.28	2.55	0.250	0.85	c)

Mg <sub>2</sub> Sn <sub>0.75</sub> Ge <sub>0.25</sub>	Mg <sub>2</sub> Sn <sub>0.73</sub> Ge <sub>0.25</sub> Sb <sub>0.02</sub>	1.4, 450 °C	3.5	162.84	1.26	0.318	2.73	c)
CoSbTe	CoSb <sub>2.85</sub> Te <sub>0.15</sub>	0.9, 550 °C	-	<sup>a)</sup> 98.73	1.94	<sup>b)</sup> 0.275	0.93	43
CoSbTeSn	CoSb <sub>2.75</sub> Te <sub>0.20</sub> Sn <sub>0.05</sub>	1.1, 550 °C	-	<sup>a)</sup> 88.33	1.05	<sup>b)</sup> 0.274	1.54	47
Ingot-BiSbTe	n.a.	1.4, 50 °C	-	<sup>a)</sup> 207.13	0.88	<sup>b)</sup> 0.168	2.64	48
Nano-BiSbTe	n.a.	1.05, 100 °C	-	<sup>a)</sup> 194.06	0.52	<sup>b)</sup> 0.184	4.58	48
Nano-BiTeSe	as-pressed Cu <sub>0.01</sub> Bi <sub>2</sub> Te <sub>2.7</sub> Se <sub>0.3</sub>	0.9, 100 °C	0.97	121.62	0.68	<sup>b)</sup> 0.11	1.31	49
PbTe-1	Tl <sub>0.02</sub> Pb <sub>0.98</sub> TeSi <sub>0.02</sub> Na <sub>0.0</sub> 2	1.7, 500 °C	-	<sup>a)</sup> 60.15	0.50	<sup>b)</sup> 0.44	3.53	50
PbTe-2	PbTe: 6% MgTe	2, 550 °C	7	56.00	0.54	<sup>b)</sup> 0.6	4.15	51
FeNbSb	FeNb <sub>0.8</sub> Ti <sub>0.2</sub> Sb	1.1, 827 °C	1.2	144.35	2.5	0.54	2.08	52

Note: a) estimated from measured  $\sigma$  and S according to the Ref. [*Chem. Mater.* 2008, **20**, 7526-7531.] , and hence no carrier effective mass  $m^*$  available; b) estimated from  $E_g = 2eS_{max}T$ ; c) this study.



**Fig. 1S.** Carrier concentration as a function of Sb content and Ge content for sample  $\text{Mg}_2\text{Sn}_{1-x-y}\text{Ge}_x\text{Sb}_y$ . It is clearly shown that the carrier concentration varies with Sb rather than Ge in  $\text{Mg}_2\text{Sn}_{1-x-y}\text{Ge}_x\text{Sb}_y$ .

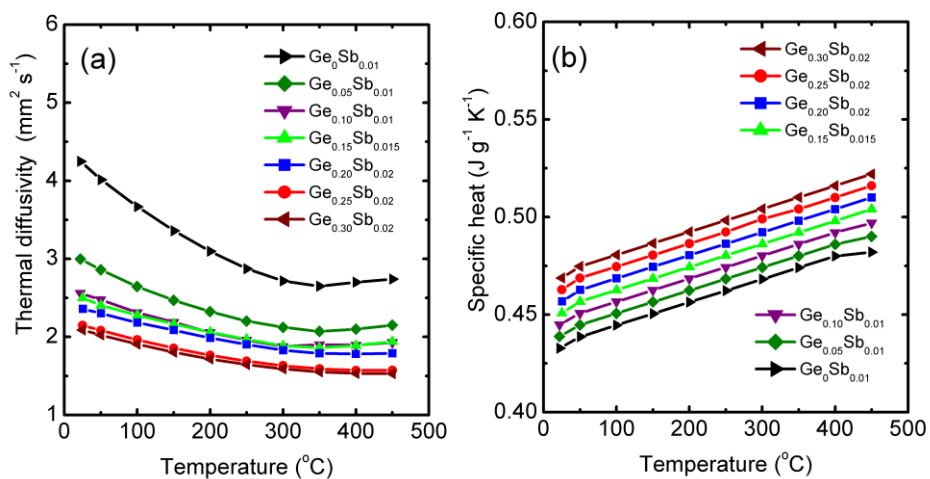


**Fig. 2S.** Temperature dependent diffusivity and specific heat of  $\text{Mg}_2\text{Sn}_{1-x-y}\text{Ge}_x\text{Sb}_y$ . (a) Thermal diffusivity, (b) specific heat.

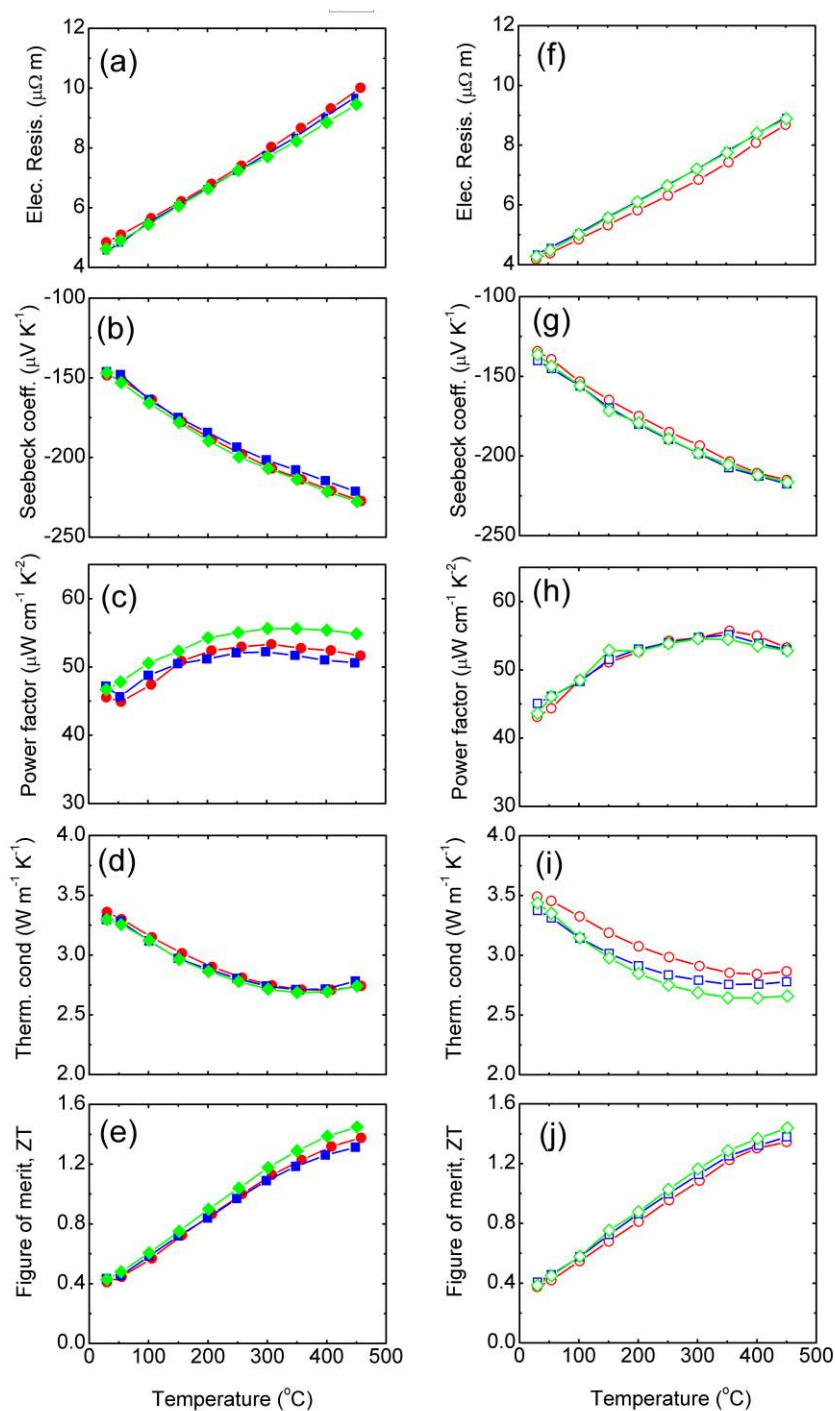


**Fig. S3.** Reproducibility of thermoelectric properties of  $\text{Mg}_2\text{Sn}_{0.75-y}\text{Ge}_{0.25}\text{Sb}_y$ . (a-e) Samples of  $\text{Mg}_2\text{Sn}_{0.73}\text{Ge}_{0.25}\text{Sb}_{0.02}$  with carrier concentration of  $2.7 \times 10^{20} \text{ cm}^{-3}$ , and (f-j) samples of  $\text{Mg}_2\text{Sn}_{0.728}\text{Ge}_{0.25}\text{Sb}_{0.022}$  with carrier concentration of  $3.0 \times 10^{20} \text{ cm}^{-3}$ .



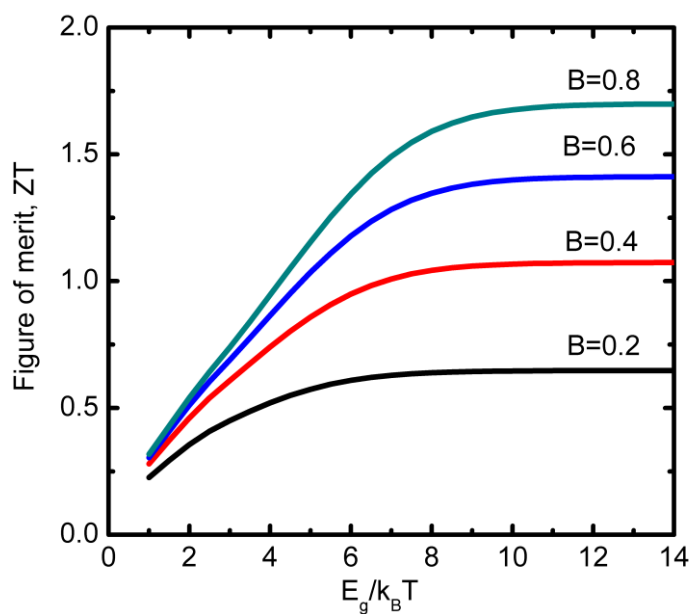


**Fig. S4.** Optimized  $ZT$  regarding with Fermi energy as a function of reduced band gap for the traditional material parameter  $B = 0.2$  (bottom curve), 0.4, 0.6, and 0.8 (top curve) for the assumption of  $s = -1/2$ ,  $\zeta_f = 0$ ,  $U_e = U_h$  and  $T = 300\text{K}$ . This shows the effect of band gap using the traditional material parameter  $B$  and is consistent with Mahan's previous work [*J. Appl. Phys.*, 1989, **65**, 1578-1583.]

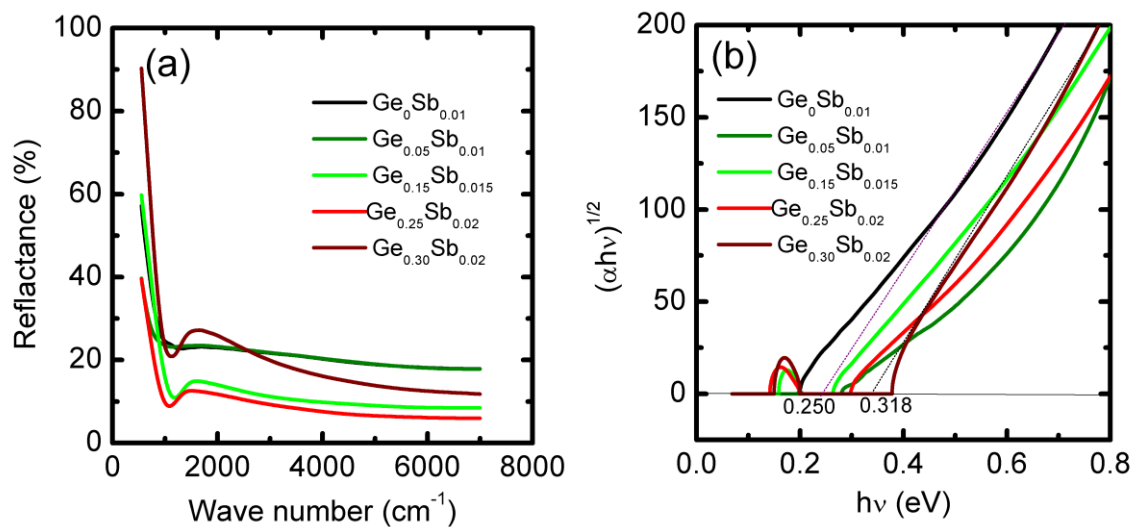


**Fig. S5.** (a) Reflectance spectrum of  $\text{Mg}_2\text{Sn}_{1-x-y}\text{Ge}_x\text{Sb}_y$ , (b) absorption spectra of  $\text{Mg}_2\text{Sn}_{1-x-y}\text{Ge}_x\text{Sb}_y$  where the across point of the dash line with  $h\nu$  axis was used to determine the band gap.

## A. Expression of ZT by using Fermi–Dirac statistics in a two-band model

We consider two simple band, i.e. one parabolic conduction band and one parabolic valence band. By applying Simon's theory [J. Appl. Phys. 33, 1830 (1962)] the electrical conductivity  $\sigma$ , Seebeck coefficient  $S$ , and thermal conductivity  $\kappa$  could expressed by the contribution of both bands as following,

$$\sigma = \sigma_e + \sigma_h, \quad (1S)$$

$$S = \frac{\sigma_e S_e + \sigma_h S_h}{\sigma_e + \sigma_h}, \quad (2S)$$

$$\kappa = \kappa_{lat} + \kappa_{carr} + \kappa_{bipolar}, \quad (3S)$$

$$\kappa_{carr} = L_e \sigma_e T + L_h \sigma_h T, \quad (4S)$$

$$\kappa_{bipolar} = \frac{\sigma_e \sigma_h}{\sigma_e + \sigma_h} (S_e - S_h)^2, \quad (5S)$$

where the subscript  $e$  and  $h$  represent the conduction band and valence band, respectively. Furthermore, the  $\sigma_i$  and  $S_i$  could be expressed by using Fermi–Dirac statistics,

$$\sigma_i = \sigma_{0,i} \frac{F_{1/2}(\xi_{f-i})}{\Gamma(3/2)}, i = e, h, \quad (6S)$$

$$S_i = \pm \frac{k_B}{e} \left( \frac{(s+5/2) F_{s+3/2}(\xi_{f-i})}{(s+3/2) F_{s+1/2}(\xi_{f-i})} - \xi_{f-i} \right), \quad (7S)$$

$$\delta_i = \frac{(s+5/2) F_{s+3/2}(\xi_{f-i})}{(s+3/2) F_{s+1/2}(\xi_{f-i})}. \quad (8S)$$

By introducing a new parameter  $\gamma = \sigma_e / \sigma_h$  for simplification and the relationships of  $\xi_{f,e} = \xi_f$  and  $\xi_{f,h} = -\xi_f - \xi_g$ , the definition of ZT, i.e.,  $ZT = S^2 \sigma T / \kappa$ , could turns into following

$$ZT = \frac{\left( \delta_e - \xi_f - \frac{\delta_e + \delta_h + \xi_g}{1+1/\gamma} \right)^2 (1+\gamma)}{\left( (B^*) \frac{F_{1/2}(\xi_f) / \Gamma(3/2)}{\xi_g} \right)^{-1} + \frac{(\delta_e + \delta_h + \xi_g)^2}{1+1/\gamma} + \left( \frac{e}{k_B} \right)^2 (L_e + \gamma L_h)}, \quad (9S)$$

$$B^* = \frac{1}{k_B} \left( \frac{e}{k_B} \right)^2 \frac{\sigma_{0,e}}{\kappa_{lat}} E_{g\_joule}, \quad (10S)$$

Eq. (9S-10S) is just the exactly form we used in main text.

---

## B. Calculation of $m^*$ from Hall coefficient and Seebeck coefficient.

5 The carrier effective mass  $m^*$  was derived from the carrier density relationship with Fermi Dirac integral,

$$n = 2 \left( \frac{2\pi m^* k_B T}{h^2} \right)^{3/2} F_{1/2}(\xi_f), \quad (11S)$$

$$F_n(\xi_f) = \int_0^\infty \frac{\chi^n}{1 + e^{\chi - \xi_f}} d\chi \quad (12S)$$

Here,  $\xi_f$  was calculated from the measured Seebeck coefficient ( $S$ ) with acoustic phonon scattering as dominant scattering  
10 mechanism, *i.e.*,  $s = -1/2$ .

$$S = \pm \left( \frac{(s + 5/2) F_{s+3/2}(\xi_f)}{(s + 3/2) F_{s+1/2}(\xi_f)} - \xi_f \right). \quad (13S)$$

The carrier concentration  $n$  was calculated from measured Hall coefficient ( $R_H$ ) and Hall factor  $r_H$ ,

15

$$n = \frac{r_H}{eR_H}, \quad (14S)$$

$$r_H = \frac{3}{2} \frac{F_{1/2}(\xi_f) F_{-1/2}(\xi_f)}{(F_{-1/2}(\xi_f))^2}. \quad (15S)$$

20

25

30

35

40

### C. Calculation of Lattice and bipolar thermal conductivity

5

Owing to the intrinsic excitation, the contribution of bipolar effect to the contribution of thermal conductivity needs to be taken into account to explain the widely observed raising tail of thermal conductivity at high temperature for most thermoelectric materials. The total thermal conductivity is composed of three parts as following,

$$\kappa_{tot} = \kappa_{lat} + \kappa_{carr} + \kappa_{bipolar} \quad , \quad (16S)$$

$$\kappa_{carr} = L\sigma T \quad , \quad (17S)$$

$$\kappa_{bipolar} = \frac{\sigma_e \sigma_h}{\sigma_e + \sigma_h} (S_e - S_h)^2 T \quad , \quad (18S)$$

where the  $\kappa_{tot}$ ,  $\kappa_{lat}$ ,  $\kappa_{carr}$ , and  $\kappa_{bipolar}$  are the total, lattice, carrier, and bipolar thermal conductivity, respectively. The Lorenz number  $L$  is Fermi energy related parameter,

$$L = \left( \frac{k_B}{e} \right)^2 \left( \frac{(s+7/2)F_{s+5/2}(\xi_f)}{(s+3/2)F_{s+1/2}(\xi_f)} - \left( \frac{(s+5/2)F_{s+3/2}(\xi_f)}{(s+3/2)F_{s+1/2}(\xi_f)} \right)^2 \right) \quad , \quad (19S)$$

15 Here, the  $s$  is the scattering parameter based on the relaxation time approximation for the electronic transport. For acoustic phonon dominant scattering mechanism,  $s$  is  $-1/2$ . The reduced Fermi energy  $\xi_f$  near room temperature could be estimated from the Seebeck coefficient on the basis of single band approximation formula Eq. (13S). The reduced Fermi energy  $\xi_f(T)$  at the higher temperature is required to solve the generalized charge neutrality equations (Eq. (20S-22S)) at a given temperature

$$20 \quad n = p_0 + N_D \quad , \quad (20S)$$

$$n = 2 \left( \frac{2\pi m_e^* k_B T}{h^2} \right)^{3/2} F_{1/2}(\xi_f) \quad , \quad (21S)$$

$$p = 2 \left( \frac{2\pi m_h^* k_B T}{h^2} \right)^{3/2} F_{1/2}(-\xi_f - \xi_g) \quad , \quad (22S)$$

For the estimation of the  $\kappa_{bipolar}$  according to Eq. (18S), we need estimated  $S_e$ ,  $S_h$ ,  $\sigma_e$  and  $\sigma_h$ . We can get  $S_e$  and  $S_h$  from Eq. (13S) by using the estimated  $\xi_f(T)$ , respectively. The estimation of  $\sigma_e$  and  $\sigma_h$  are based on the calculated carrier concentration and the fitting carrier mobility.  $m_e^*$  was obtained from the measured carrier concentration and Seebeck coefficient of  $\text{Mg}_2\text{Sn}_{1-x-y}\text{Ge}_x\text{Sb}_y$  in this study, while  $m_h^* = 1.3 m_0$  was used according to the Ref. [V. K. Zaitsev, CRC Press, New York, 2005].  $\mu_e$  was estimated from  $(\sigma_e + \sigma_h)/(e(n+p))$ , while  $u_h$  was used to fitting the temperature dependent  $\sigma$  and  $S$ . The temperature coefficient of the band gap of  $\text{Mg}_2\text{Sn}_{1-x-y}\text{Ge}_x\text{Sb}_y$  were estimated from interpolation between the reported value for  $\text{Mg}_2\text{Sn}$  ( $dE_g/dT = 3 \times 10^{-4} \text{ eV/K}$ ) and  $\text{Mg}_2\text{Ge}$  ( $dE_g/dT = 1.8 \times 10^{-4} \text{ eV/K}$ ) from Ref. [V. K. Zaitsev, CRC Press, New York, 2005]. The effect of the dopant Sb and extra Mg on the  $dE_g/dT$  was neglected.

30

## D. Calculation of band gap from the Fourier transform infrared spectrum

The Fourier transform infrared spectrums of selected samples were measured to derive the optical band gap. For near-normal incidence, the complex refractive index  $n(\omega)$  and the extinction coefficient  $k(\omega)$  with both the real and imaginary parts can be obtained from the Kramers-Kronig analysis as following,

$$n(\omega) = \frac{1 - R(\omega)}{1 + R(\omega) - 2[R(\omega)]^{1/2} \cos[\Theta(\omega)]}, \quad (23S)$$

$$k(\omega) = \frac{2[R(\omega)]^{1/2} \sin[\Theta(\omega)]}{1 + R(\omega) - 2[R(\omega)]^{1/2} \cos[\Theta(\omega)]}, \quad (24S)$$

where  $\Theta(\omega)$  is the phase shift, which is,

$$\Theta(\omega) = \frac{\omega}{\pi} \int_0^{\infty} \frac{\ln[R(\omega')] - \ln[R(\omega)]}{\omega'^2 - \omega^2} d\omega'. \quad (25S)$$

The extinction coefficient  $k(\omega)$  is used to calculate the frequency dependent absorption coefficient  $\alpha(\omega)$  through the relation,

$$\alpha(\omega) = 4\pi\omega k(\omega). \quad (26S)$$

Finally, the  $(\alpha hv)^{1/2}$  was plotted as a function of the energy  $hv$ , as shown in Fig. S7. The across point of the dash line with  $hv$  axis was used to determine the band gap

## E. Connections among the components of $B^*$

It is worthy pointing out that the components ( $U^*$ ,  $E_g$ , and  $\kappa_{lat}$ ) determining the material parameter  $B^*$  are still interconnected with each other from a more fundamental point of view. Here, we show a simple discussion about the deeper relation between  $U^*$  and  $E_g$ . Firstly, Let us to recall the definition of  $U^*$  in the main body ,

$$U^* = \mu (m^*/m_0)^{3/2} T^{3/2} \quad (S27)$$

Then, we replace the carrier effective mass term  $(m^*)^{3/2}$  in the definition of  $U^*$  with  $N_v(m_b^*)^{3/2}$  where  $m_b^*$  and  $N_v$  are the band effective mass  $m_b^*$  and the number of degenerate band valley  $N_v$ , respectively.

$$U^* = \mu N_v (m_b^*/m_0)^{3/2} T^{3/2} \quad (S28)$$

Considering the acoustic phonon as dominant carrier scattering mechanism for most thermoelectric materials,  $\mu$  in Eq. (S28) could be further evolved using the deformation potential  $E_d$ , elastic constant  $C_l$  (Similar treatment could be found in Ref. 9.), and then Eq. (S27) turns into,

$$U^* \propto \frac{N_v C_l}{(m_b^*/m_0)} E_d \quad (S29)$$

According to Eq. S29, a larger  $N_v$  and smaller  $m_b^*$  are favorable for higher  $U^*$ . Now the material parameter  $B^*$  could be rewritten as,

$$B^* \propto \frac{N_v C_l}{E_d \kappa_{lat}} \frac{E_g}{(m_b^*/m_0)} \quad (\text{S30})$$

Based on the k·p perturbation theory,  $m_b^*$  is related to  $E_g$ , conduction band wave function  $\Gamma_c$ , and valance band wave function  $\Gamma_v$ .

$$\frac{1}{m_b^*} = \frac{1}{m_0} + \frac{2|\langle \Gamma_c | k \cdot p | \Gamma_v \rangle|^2}{m_0^2 k^2 E_g} \quad (\text{S31})$$

5 This relation essentially describes the fact that the effective mass of a free electron in one band changes due to the coupling to the electrons in other bands. For non-degenerate conduction band electrons, it has been shown that a material with larger  $E_g$  usually has a heavier  $m_b^*$  that corresponds to a lower mobility, according to Ref. 55. According to the data for typical V (Ge), III-V (GaN, GaAs, GaSb, InP, InP and InAs), II-VI (ZnS, SnSe, ZnTe, CdTe) semiconductor, the ratio of  $E_g/(m_b^*/m_0)$  decreases with increase of band gap. This simplified picture partly explains why most of the well-known thermoelectric  
10 materials are narrow band semiconductor. However we want to caution that for thermoelectric materials where heavy atoms are usually involved, spin-orbit coupling needs to be considered and the above formalism needs to be carefully examined with more details. Additionally, the controllable doping for many semiconductors with wide band-gap are still a technical challenge which also prevents people from more widely investigating their thermoelectric performance. Further explorations into the relation among the parameters in generalized material parameter  $B^*$ , described in Eq. S28, would be  
15 more insightful to guide the researcher to atomically construct ideal materials with optimized atomic sizes, bonding strengths, and crystalline structures.

#### F. Estimated $U^*$ from measured $S$ and $\sigma$

For the samples without data from Hall measurement in the Table S1, including CoSbTe, CoSbTeSn, ingot-BiSbTe, nano-  
20 BiSbTe, and PbTe-1,  $U^*$ s were estimated from the measured Seebeck coefficient  $S$  and electrical conductivity  $\sigma$  at room temperature as following,

$$S = \pm \frac{\kappa_B}{e} \left( \left( s + \frac{5}{2} \right) - \xi_f \right) \quad (\text{S32})$$

$$\sigma = 2e \left( \frac{2\pi m_0 k_B T}{h^2} \right)^{3/2} (m^*/m_0)^{3/2} \mu \exp(\xi_f) = A \cdot U^* \exp(\xi_f) \quad (\text{S33})$$

Here,  $A$  is a constant for simplification,

$$25 \quad S = \pm \frac{\kappa_B}{e} \left( \left( s + \frac{5}{2} \right) + \ln A + \ln U^* - \ln \sigma \right) \quad (\text{S34})$$

$$20 \quad U^* = \exp \left\{ \left( |S| \frac{e}{\kappa_B} \right) + \ln \sigma - \left( s + \frac{5}{2} \right) + \ln A \right\} \quad (\text{S35})$$

The error bar for  $U^*$  by using this method should be similar to that of the term  $\mu(m^*/m_0)^{3/2}$ , which has been discussed in *Chem. Mater.* 2008, **20**, 7526-7531.